Lawrence Berkeley National Laboratory
Recent Work

Title
DEVELOPMENT OF ANODE ALLOYS FOR: ALUMINUM/AIR BATTERIES: FINAL REPORT

Permalink
https://escholarship.org/uc/item/4z60t3tv

Authors
Macdonald, D.D.
Real, S.
Urquidi-Macdonald, M.

Publication Date
1988-04-01

Lawrence Berkeley Laboratory

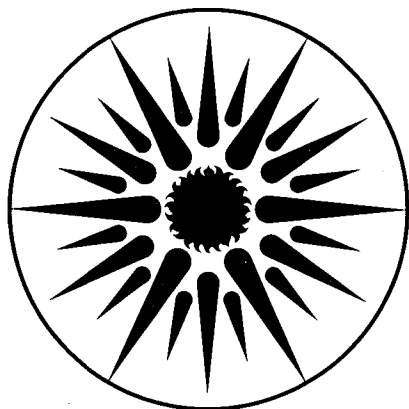## UNIVERSITY OF CALIFORNIA

APPLIED SCIENCE DIVISION

Development of Anode Alloys for Aluminum/Air Batteries: Final Report

D.D. Macdonald, S. Real, and M. Urquidi-Macdonald

April 1988

TWO-WEEK LOAN COPY

*This is a Library Circulating Copy
which may be borrowed for two weeks.*

**APPLIED SCIENCE
DIVISION**

DISCLAIMER

DEVELOPMENT OF ANODE ALLOYS
FOR ALUMINUM/AIR BATTERIES

Final Report

April 1988

by

Digby D. Macdonald
Silvia Real
Mirna Urquidi-Macdonald

SRI International
333 Ravenswood Avenue
Menlo Park, California   94025-3493

for

Technology Base Research Project
Applied Science Division
Lawrence Berkeley Laboratory
University of California
Berkeley, California   94720

SUMMARY

The electrochemistry of various Al-Li-In, Al-Li-In-Bi, and Al-Mg-Mn-In alloys in 4 M KOH at 50°C has been investigated by delineating the partial anodic and cathodic processes as a function of potential.

The Al-Li-In alloys (Group 1) and the Al-Li-In-Bi alloys (Group 2) exhibit high corrosion rates under open circuit conditions and do not display activation phenomena as the potential is swept in the negative to positive direction. Accordingly, these alloys are judged to be unsuitable as fuels for alkaline aluminum/air batteries. The Al-Mn-Mg-In alloys (Group 3) do exhibit activation at potential within the range -1.75 to -1.85 V (vs Hg/HgO, 4 M KOH) as a result of oxidation of manganese from the surface to form a soluble product. These alloys display significantly lower open circuit corrosion rates. All the alloys in this group passivate at more positive potentials, followed by a region over which the current varies nearly linearly with voltage. These same characteristics are exhibited by Alloy BDW (Al-1Mg-0.1 In-0.2 Mn), which we investigated previously. However, none of the alloys studied in the present program appears to offer any advantages over Alloy BDW as a fuel for alkaline aluminum/air batteries.

We have also continued to analyze various mechanisms to account for the extensive electrochemical impedance data for pure aluminum in 4 M KOH at 25°C that we reported previously. Six mechanisms were explored, including some that involve autocatalytic steps in the aluminum electrodissolution process. None of these mechanisms appears to be capable of accounting for the measured impedance any better than the simple irreversible coupled dissolution/hydrogen ion-atom evolution mechanism reported earlier. Although these latter mechanisms can explain the inductive behavior at intermediate frequencies, in terms of the autocatalytic reactions, they do not seem to explain other features of the impedance as a function of frequency and applied potential, nor do they account for the steady-state partial anodic and cathodic current/voltage curves.

CONTENTS

TABLES

I INTRODUCTION

Aluminum/air batteries are being actively developed as power sources for automobiles and for some stationary applications (1-7). The advantages offered by these power sources include near-ambient temperature of operation (50° to 80°C), mechanical recharging, high power density (up to 800 mW/cm^2 peak), high energy density fuel (aluminum is second only to lithium in this regard), and the use of air as the oxidant. Additionally, aluminum is nontoxic, easily handled, and is readily available. The existing manufacturing base is sufficient to supply the necessary fuel for more than a million vehicles.

A key aspect of the Al/air system is mechanical recharging. The battery can be recharged with tens of kiloampere-hours of energy in a few minutes, in a manner that is analogous to refueling a vehicle powered by an internal combustion engine. Electrically recharged systems require several orders in magnitude more time to deposit that same amount of energy into the battery. Perhaps the most important characteristic is that mechanical recharging eliminates the problems of dendrite growth and anode shape change that have plagued other (electrically recharged) metal/air batteries (e.g., Zn/air). Thus, in principle, recharging does not limit the future cycle life of the battery, a feature that is more characteristic of a fuel cell than of a rechargeable battery.

The aluminum/air battery is not without problems. The principal drawbacks are that it may require fairly sophisticated electrolyte and thermal management systems to remove the reaction products [Al(OH)$_3$ and heat], the fuel corrodes on standby and during discharge, and the fuel is more expensive than gasoline (about $3/gallon equivalent). The often-cited need to recycle the reaction product to convert it into aluminum is also a potential source of problems, particularly if minor alloying elements (such as Tl, Ga) interfere with the Hall process. However, the arguments for recycling are not particularly convincing, unless the number of aluminum/air powered vehicles in use becomes a significant fraction of the total automobile fleet. Nevertheless, it is

1

an issue that must be kept in mind when developing fuels for aluminum/air batteries.

Corrosion of the aluminum alloy fuel is a matter of major concern in aluminum/air battery technology because corrosion reduces the energy density on standby and reduces the power density and current efficiency during operation. Work by Despic (5) and by others (1,7) showed that it was necessary to alloy aluminum with minor constituents (e.g., Ga, In, Tl) in order to "poison hydrogen evolution," and hence to reduce the corrosion rate to an acceptable level. However, this early work did not show, unequivocally, that hydrogen evolution was indeed preferentially inhibited, and some of the data indicate that inhibition of the anodic reaction also occurs, with possibly serious consequences on the power density of the battery.

Over the past five years, through the support of both ELTECH Systems and the Department of Energy (Subcontract No. 100484-MLM), we have synthesized about sixty aluminum anode alloys, evaluated their corrosion resistance, correlated the corrosion behavior with alloy composition, and investigated the mechanisms by which minor alloying elements can have such a profound effect on the electrochemistry of the alloys in concentrated hydroxide media. These studies (8-13), which are summarized in Section II, necessitated the development of unique experimental techniques for delineating the anodic and cathodic partial reactions. Furthermore, we used wide—bandwidth electrochemical impedance spectroscopy (EIS) to define the mechanisms of the electrodissolution of the alloy and hydrogen evolution and to determine the mechanistic roles of the minor alloying elements. These studies have allowed us to formulate a mechanism for the activation/deactivation of aluminum anodes in concentrated hydroxide media, and we are now able to predict which alloying elements should be most effective. This follow-on study extends our work to further define the mechanism(s) for the electrodissolution of additional classes of aluminum alloys and to use this knowledge to prepare and evaluate new anode alloys for aluminum/air batteries.

II PREVIOUS WORK

A. Corrosion

In our previous studies (8,13), we prepared two series of alloys for both fundamental corrosion studies and evaluation in benchscale aluminum/air batteries. The corrosion studies were designed to explore the effectiveness of various alloying elements in inhibiting open circuit corrosion of aluminum alloys (Table 1) in concentrated hydroxide media at temperatures ranging from 25° to 80°C. Both the hydrogen evolution rate and the rate of weight loss were measured, and a good correlation (in accordance with Faraday's law) was found between the two parameters (Figure 1). Additions of gallium, indium, and zinc alone were found to increase the corrosion rate, with the effect being greatest for Ga. Bismuth and tellerium had little effect (Figure 1). However, the addition of two or more elements frequently had a dramatic inhibitory effect, in some cases reducing the open circuit corrosion rate by more than a factor of 20 over pure aluminum and more than 100 over the commercial alloy RX-808.

A weak, but nevertheless significant, correlation was found to exist between the corrosion rate and the open circuit potential (Figure 2), such that the corrosion potential becomes more positive as the corrosion rate is lowered. This trend is consistent with inhibition of the anodic partial reaction rather than with poisoning hydrogen evolution. Of particular significance in Figure 2 is the group of alloys (Nos. 14, 15, 16, 20, 21) that exhibit very low corrosion rates and yet display quite negative open circuit potentials. At the outset of the current work, we adopted the definition of a "practical" alloy as being one that exhibits approximately the same open circuit corrosion rate as pure zinc under the same conditions. Alloy 20, with a corrosion rate of 0.041 mg/cm^2/ min, is within a factor of 30 of this goal and is more than a factor of 100 lower than that exhibited by RX-808. However, all the alloys in this group contain thallium, which renders them unacceptable for environmental reasons.

3

Table 1

RESULTS OF OPEN CIRCUIT POTENTIAL AND CORROSION RATE MEASUREMENTS ON VARIOUS ALUMINUM ALLOYS IN 4 M KOH AT 50°C

Alloy	Composition (Nominal)	OCP* (mV Hg/HgO)	Corrosion Rate (mg/cm²/min)	Hydrogen Evolution Rate (ml/cm²/min)	Remarks
Al	99.99%	-1678	0.515	0.726	Alcoa
Al	99.999%	-1675	0.876		Alfa
Al	Alcoa 1100-H14	-1250	2.735		Supplied by DSC
RX-808	0.67% Ga	-1825	6.832	9.163	
	0.815% Mg				
Zn		-1400	0.0014	0.00496	
Z1	0.1% Zn	-1510	1.030	1.490	
Z2	0.5% Zn	-1510	1.074	1.531	
Z3	1.0% Zn	-1525	1.097	1.569	
Z4	5.0% Zn	-1540	1.190	1.703	
B1	0.1% Bi	-1840	0.593	0.879	
B2	0.5% Bi	-1830	0.461	0.668	
B3	1.0% Bi	-1860	0.520	0.748	
B4	5.0% Bi	-1830	0.507	0.689	
T1	0.01% Te	-1650	0.525	0.779	
T2	0.05% Te	-1640	0.584	0.863	
T3	0.1% Te	-1640	0.523	0.759	
T4	0.5% Te	-1640	0.529	0.762	
I1	0.01% In	-1700	1.910	2.799	
I2	0.05% In	-1715	2.287	3.330	
I3	0.1% In	-1740	1.965	2.894	
I4	0.5% In	-1740	2.106	3.046	
G1	0.01% Ga	-1790	8.740	11.948	
G2	0.05% Ga	0-1820	5.707	8.110	
G3	0.1% Ga	-1800	5.845	8.217	
G4	0.5% Ga	-1810	7.627	9.856	
Pb1	0.5% Pb	--	0.736	--	
P1	0.5% P	--	0.846	--	P_2O_5 burnt out

*Open circuit potential.

Table 1 (Concluded)

Alloy	Composition (Nominal)	OCP* (mV Hg/HgO)	Corrosion Rate (mg/cm²/min)	Hydrogen Evolution Rate (ml/cm²/min)	Remarks
No. 11	0.2% P	-1750	0.918		
No. 12	0.2% P(AlP₄)	-1670	0.763		
No. 13	0.1% P 0.2% Ga	-1800	153.4		
No. 14	0.1% P 0.1% In 0.2% Ga 0.01% Tl	-1725	0.057		
No. 15	0.1% P 0.1% In 0.2% Ga 0.01% Tl	-1750	0.058		99.99% Al
No. 16	0.2% Ga 0.07% In 0.01% Tl	-1680	0.051		
No. 17	0.05% In 0.01% Tl	-1720	0.980		
No. 18	0.05% In 0.05% Tl	-1737	0.733		
No. 19	0.2% In 0.05% Tl	-1725	0.0621		
No. 20	0.25 In 0.1% Tl 0.01% Ga	-1610	0.041		
No. 21	0.1% In 0.1% Tl 0.2% Ga	-1625	0.048		

*Open circuit potential.

The bismuth-containing binaries B_1-B_4 (0.1 to 5% Bi) also show considerable promise, although they do not exhibit corrosion resistance superior to that of pure aluminum. These alloys exhibit remarkably negative open circuit potentials and corrosion resistances that are far superior to the commercial alloy RX-808, which was an early contender as a fuel for aluminum/air batteries. If the corrosion rates of the B_1-B_4 series could be lowered by a factor of ten, while maintaining the open circuit potentials at their present values, they might be significantly better anode fuels than any alloys currently known.

An important feature of the data plotted in Figures 1 and 2 is that neither the corrosion rate nor the open circuit potential strongly correlates with the composition. Thus, in the B_1-B_4 series, the alloy containing 0.1% Bi is just as effective as that containing 5% Bi. This observation is extremely important , because it gives the alloy designer considerable flexibility in fabricating anode fuels, significantly decreases the problem of constituent toxicity, and lowers the cost.

A second feature of these data, which has been noted previously (5,7), is that strong synergistic effects apparently exist between different alloying elements. Thus, indium, gallium, and thallium do not inhibit corrosion when individually in aluminum, but when added together, they greatly decrease the corrosion rate. In our view, this synergism is the key to designing aluminum anodes for Al/air batteries. A principal objective of our future work is to develop a mechanistic understanding of the origin of the synergistic effect.

B. Alloy Activation

During our previous work (9,10), we developed experimental techniques for delineating the partial anodic and cathodic (hydrogen evolution) reactions during the polarization of aluminum alloys in alkali media. Briefly, this delineation was achieved by oxidizing the evolved hydrogen downstream in a porous nickel (Pt activated) anode, details of which are given in our last report (12). This technique proved to be a key development because it allowed us to examine, separately, the current/voltage characteristics of the anodic and cathodic processes. These characteristics, in turn, led to very

6
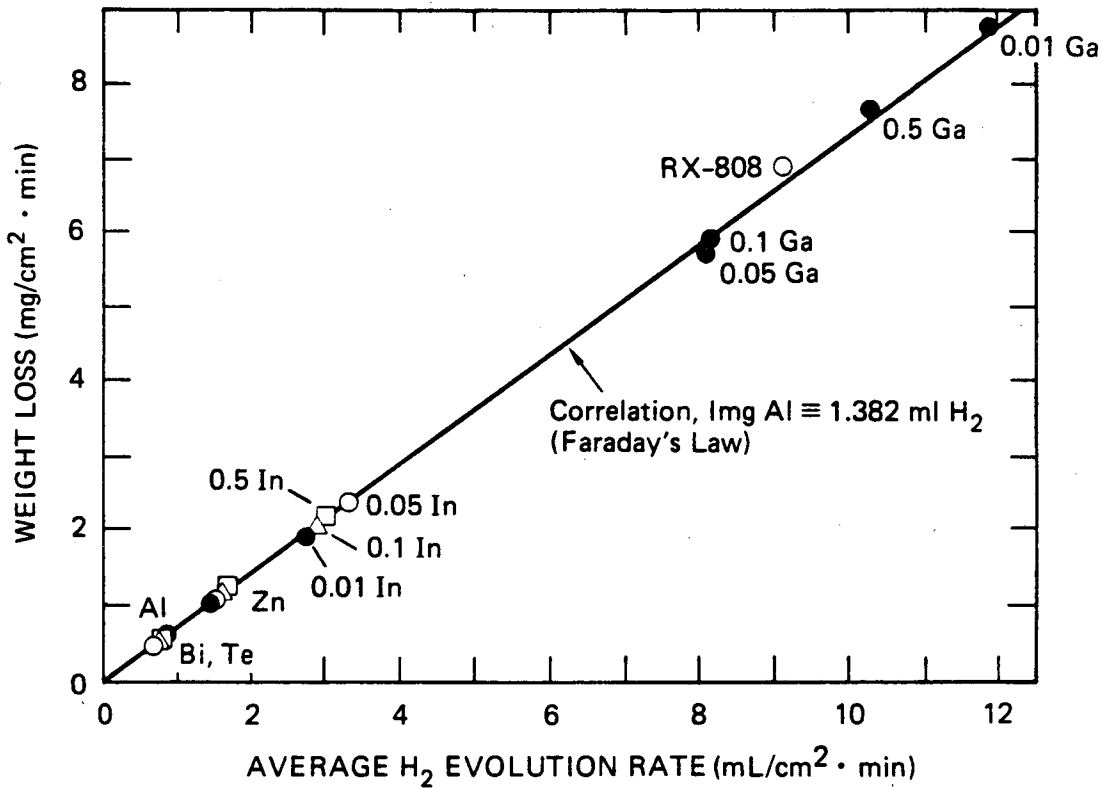
Figure 1. Correlation between corrosion rate (weight loss) and hydrogen evolution rate for the various binary alloys evaluated in 4 M KOH at 50°C.

7
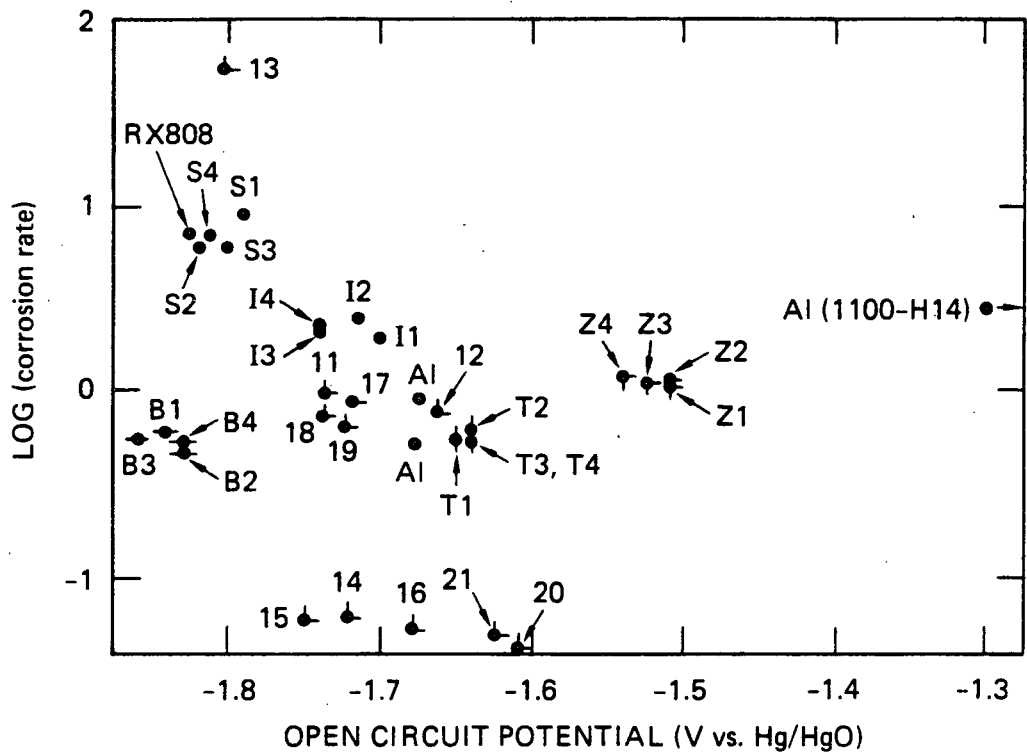
Figure 2.   Plot of log (corrosion rate) versus open circuit potential for various alloys in
4 M KOH at 50°C.

The compositions of the alloys are identified in Table 1.

RA-320583-40

important discoveries concerning the electrochemistry of aluminum alloys in alkali media.

An example of this type of analysis for pure aluminum in 4 M KOH at 25°C is shown in Figure 3. Although the total current indicates that aluminum is an active metal in this medium (i.e., no apparent passivation phenomena), the delineated anodic partial current leads to a quite different conclusion. Thus, with reference to Figure 3, it is apparent that aluminum is a _passive_ metal, with the tail end of the active-to-passive transition being observed at -1.95 to -1.85 V. The current then remains constant to about -1.6 V, but at more positive potentials it increases almost linearly with voltage.

Similar phenomena are observed at 50°C (Figure 4), but at 80°C (Figure 5) the rates of all reactions are so high that it has not been possible to displace the potential to a sufficiently negative value to detect the passive state (if it exists).

The linear current/voltage region shown in Figures 3 through 5 is similar to that observed for zinc (14), and is characteristic of dissolution through a surface film of constant resistance. The formation of corrosion product films on aluminum in hydroxide solutions has been noted by others (15-17) and is expected on purely thermodynamic grounds (18). As in the case of zinc in sodium hydroxide solution (14), it is within this linear I/V region that the anode discharges during operation of the battery, so that these current/voltage characteristics ultimately determine the power density of the anode. Clearly, the aluminum anode operates in the transpassive dissolution mode, a finding that is of some significance for mechanistic studies.

The corresponding current/voltage curves for Alloy 20 at 25°C, 50°C, and 80°C are shown in Figures 6, 7, and 8, respectively. In these cases, the current/voltage characteristics are quite different from those exhibited by pure aluminum. First, the alloy exhibits "passive" behavior over a wide potential range of almost 500 mV, a range which comparable to that shown by stainless steels in acid solutions. Second, the alloy activates almost discontinuously over a small range of

9
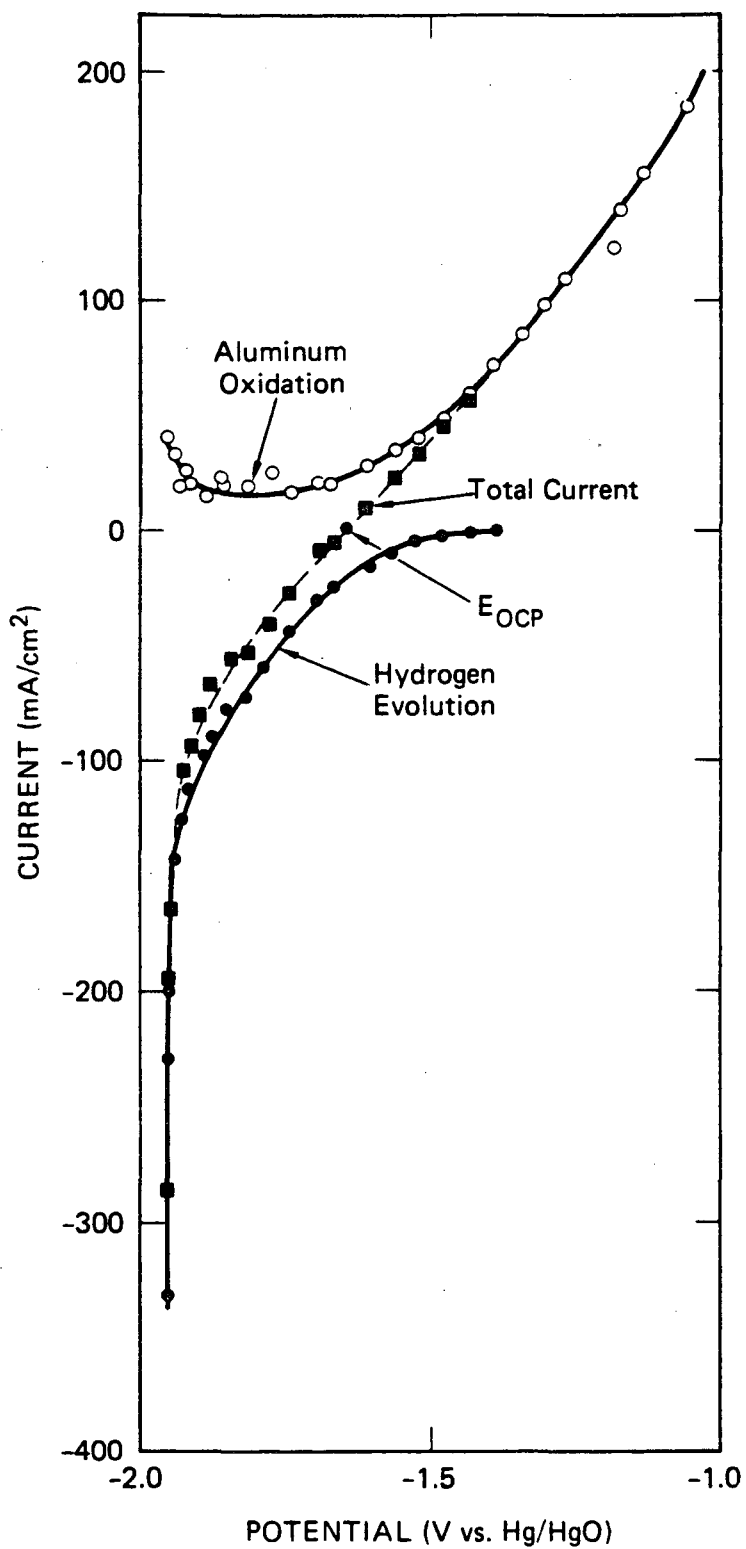
Figure 3. Steady state polarization curve for pure aluminum in 4 M
KOH at 25°C showing the total current and the anodic and
cathodic partial currents.
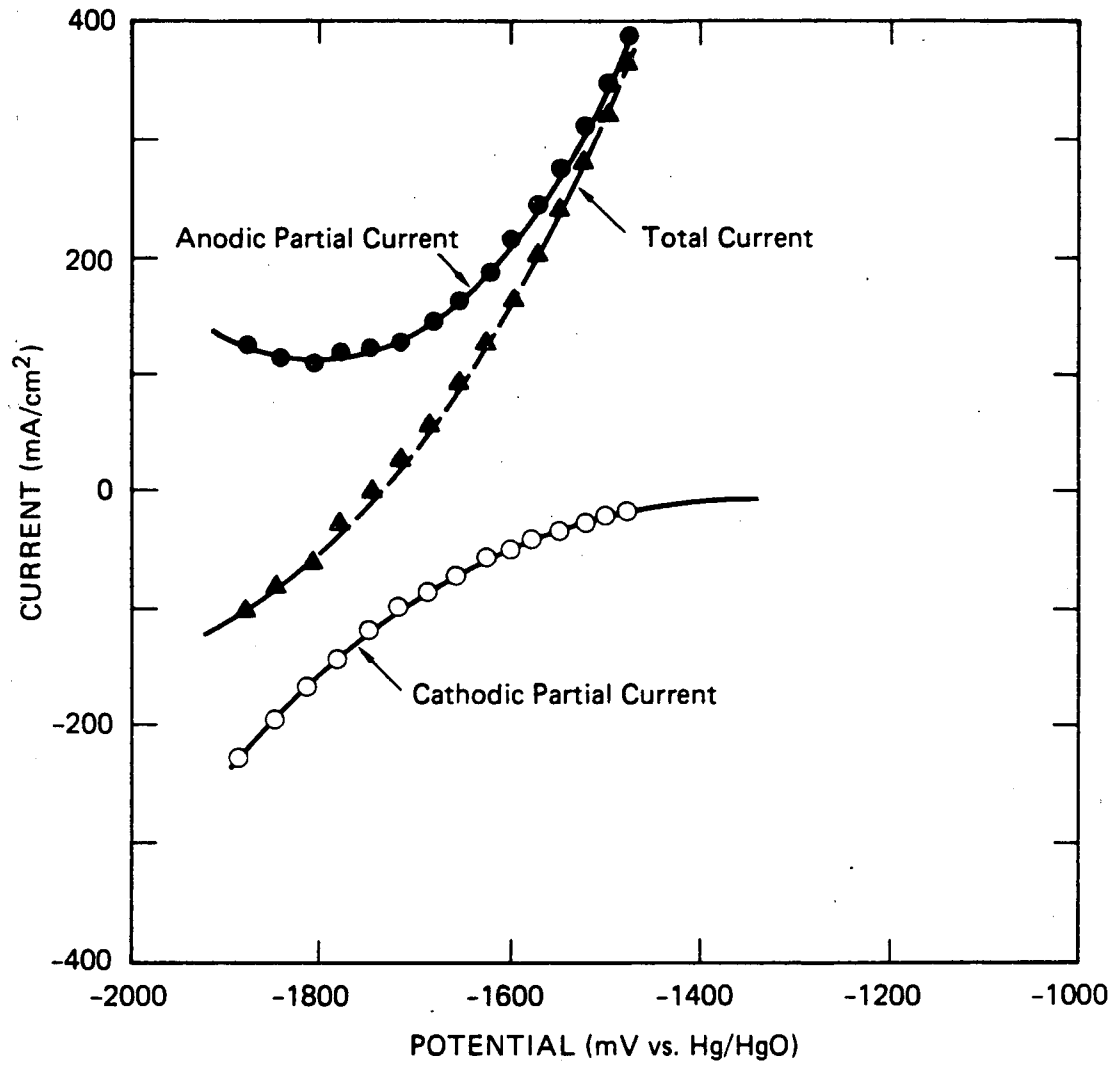
Figure 4. Steady state polarization curve for pure aluminum in 4 M KOH at 50°C showing the total current and the anodic and cathodic partial currents.

RA-m-320583-41

11
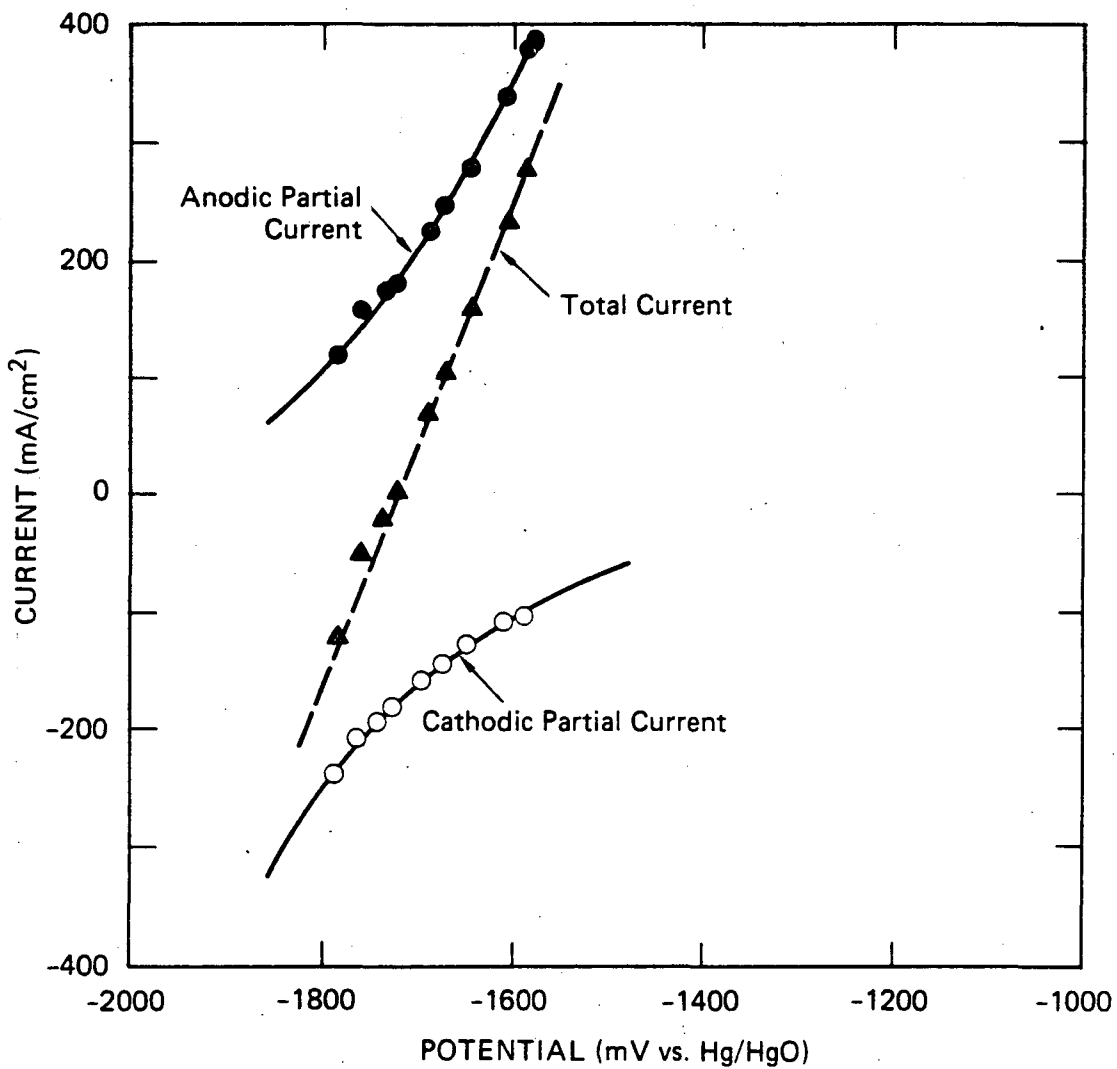
Figure 5. Steady state polarization curve for pure aluminum in 4 M KOH at 80°C
showing the total current and the anodic and cathodic partial currents.
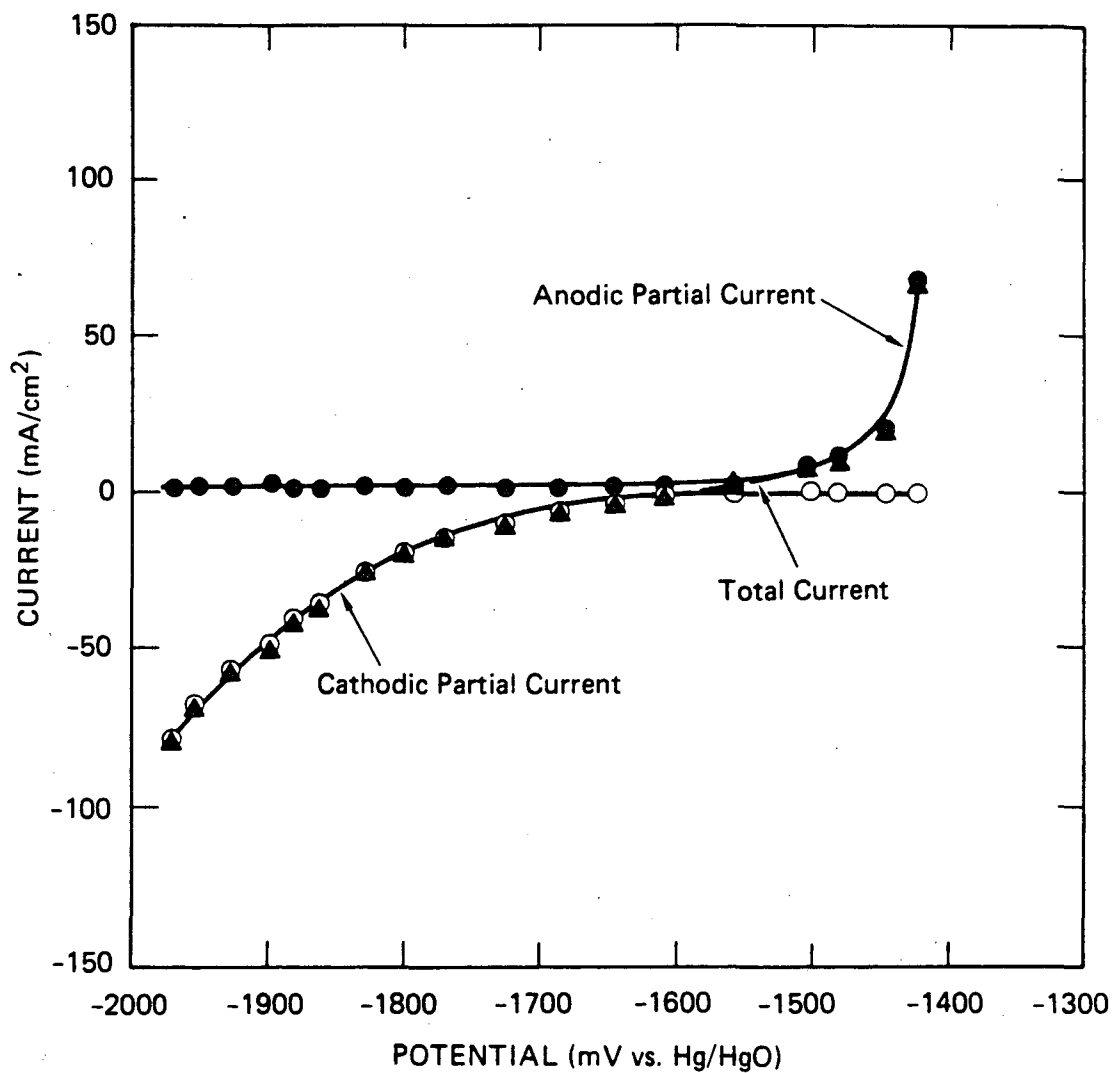
RA-m-320583-42

RA-m-320583-43

Figure 6. Steady state polarization curve for Alloy No. 20 in 4 M KOH at 25°C showing the total current and the anodic and cathodic partial currents.

13
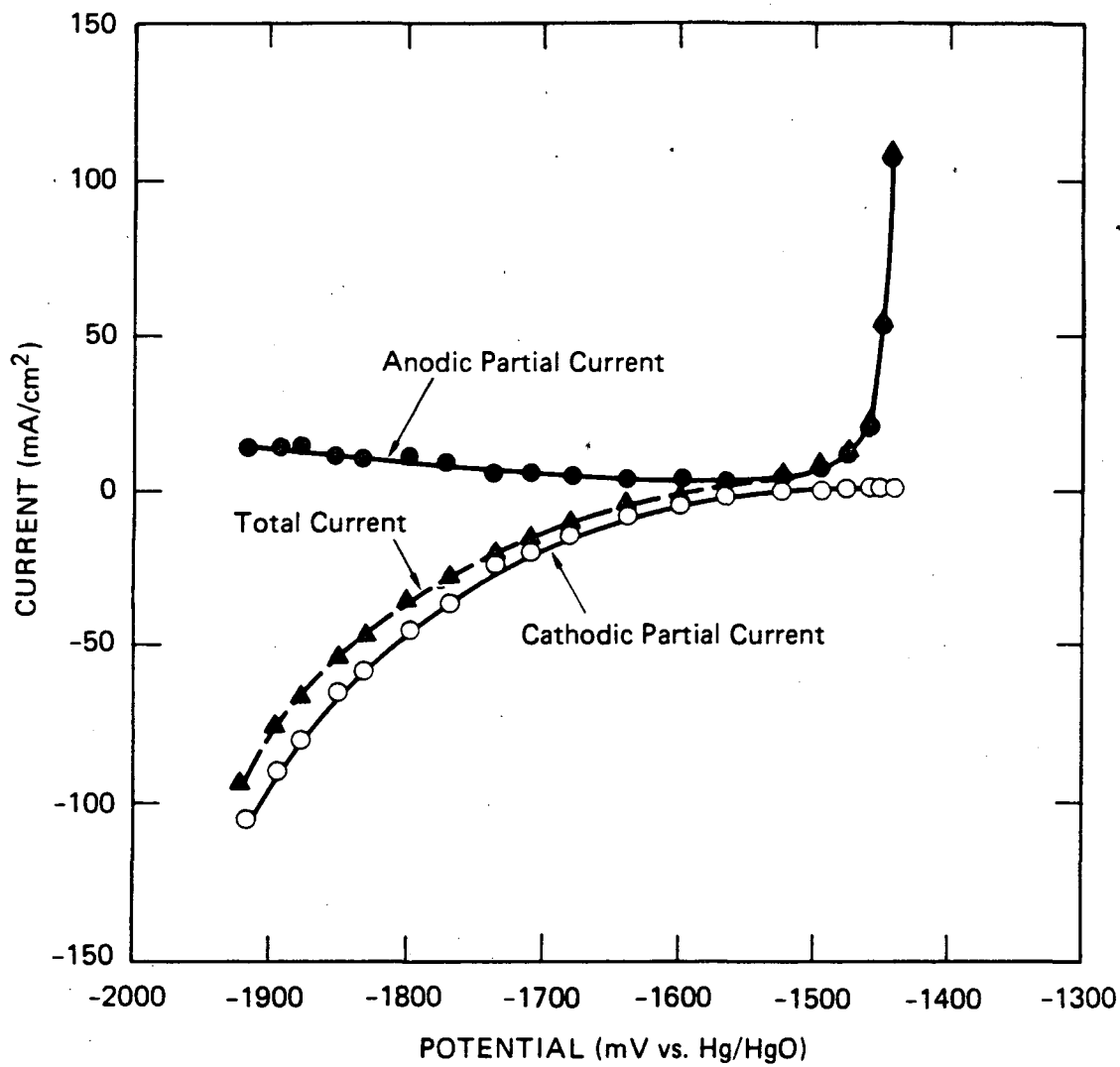
Figure 7. Steady state polarization curve for Alloy No. 20 in 4 M KOH at 50°C showing the total current and the anodic and cathodic partial currents.

RA-m-320583-44

14
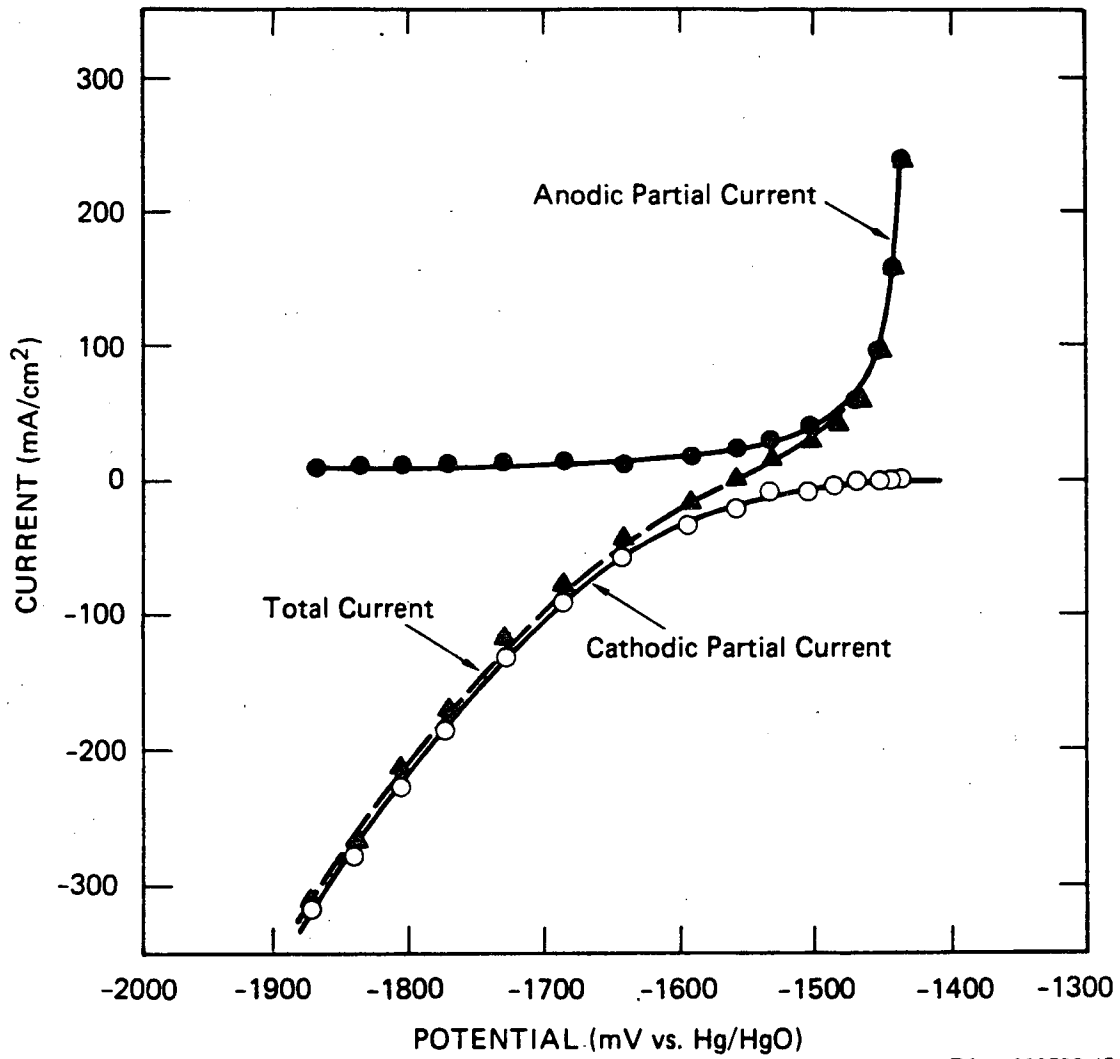
Figure 8. Steady state polarization curve for Alloy No. 20 in 4 M KOH at 80°C showing the total current and the anodic and cathodic partial currents.

RA-m-320583-45

potential at about -1450 mV. This discontinuity cannot be explained by the electrodissolution of a <u>bulk</u> phase (e.g., of the base metal), but rather we suggest that the observed breakdown results from the oxidative removal of a thin surface layer of the alloying element(s) as the potential is swept in the negative-to-positive direction. At higher potentials, the current/voltage characteristics are determined essentially by the electrochemical properties of the base aluminum alloy, which may or may not coincide with those of pure aluminum.

We have assembled the ideas developed above into a relatively simple model for the activation of aluminum alloy anodes (Figure 9). In this model, the anode can exist in one of two states: the "passive" state under standby or the "transpassive dissolution" state during discharge. The performance of the alloy during standby is measured directly in terms of the corrosion current (I_{corr}), whereas during the operating period, the performance is indicated by the discharge current (I_d) and voltage (E_d), the product of which is a measure of the power density of the fuel. At the higher temperatures of interest (50°C and 80°C), the current/voltage curves for both pure aluminum (Figure 5) and the alloy (Figure 8) in the operating region (Figure 9) are very steep, so that the discharge voltage (E_d) most likely lies quite close to E_{crit}, unless the anode is being discharged under very high rate conditions.

Accordingly, we propose that the two most important parameters that characterize an anode alloy are I_{corr} (corrosion rate under standby conditions) and E_{crit}, which essentially determines the voltage at which the anode will discharge. Clearly, a superior alloy is one that has a low I_{corr} and a very negative critical activation potential (E_{crit}).

The synergistic effect referred to above is observed on alloys in the standby state and is displayed in terms of the corrosion current I_{corr} (equivalent to the corrosion rate). This phenomenon has a profound effect on the corrosion current, and even very small amounts of an element are able to exert a significant change in I_{corr}. The alloying element(s) also determine E_{crit}, but in this case there is little evidence of a synergistic effect. Rather, the critical potential

16
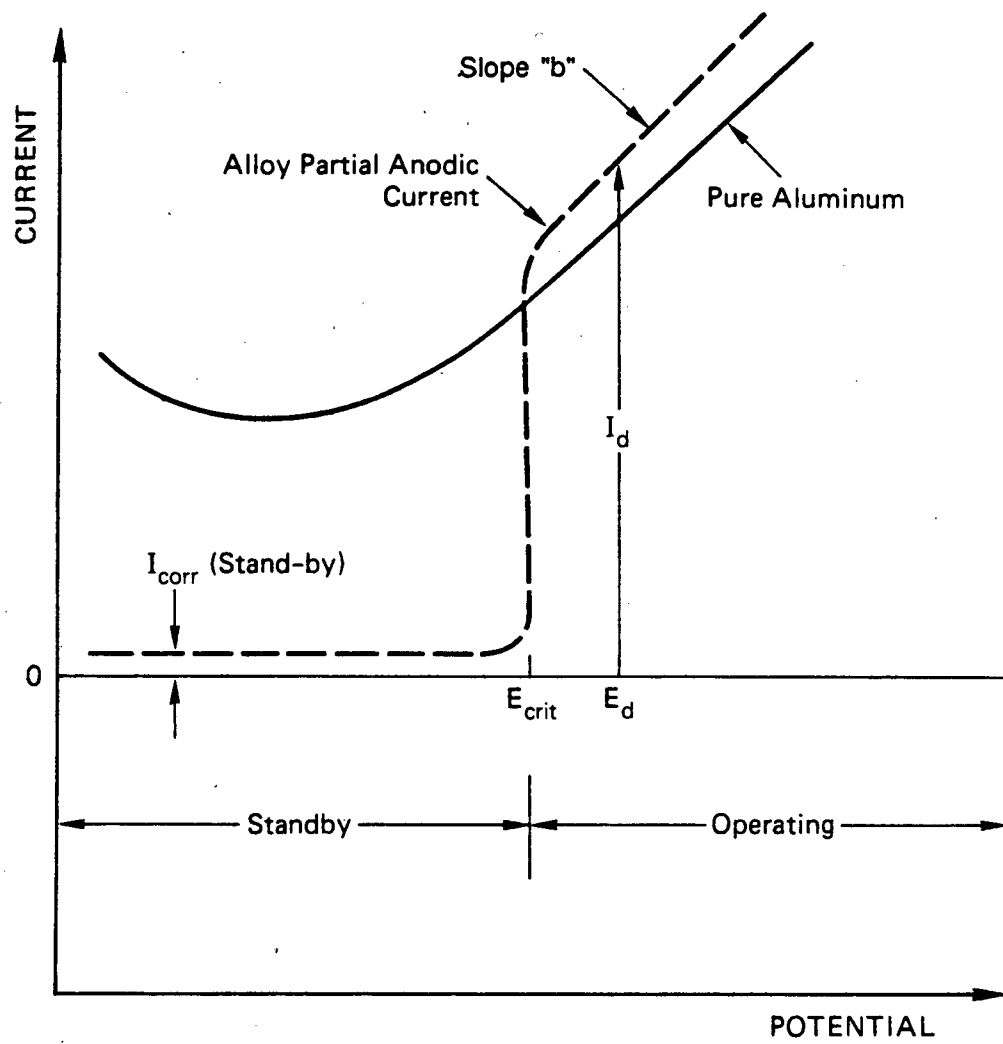
Figure 9. Model for activation/deactivation of aluminum anodes in Al/air batteries.

17

appears to be determined by the oxidation characteristics of one of the alloying elements.

At the current time, we have little information on the structure or chemical properties of the species that are responsible for the strong passivation of the surface (Figures 5 and 8), but we may surmise some of the processes by which the protective layer forms. First, we know from the early work of Cooper (1), and from our own studies (13), that the addition of stannate to the electrolyte causes a similar passivation of the anode under standby conditions and yet does not adversely affect the discharge characteristics. Furthermore, the stannate is reduced to metallic tin at the anode surface, and our low frequency impedance studies (19) indicate that it forms as a porous layer. Second, on the basis of the alloy composition, the inhibiting component(s) must be concentrated at the surface in a way that renders the effect insensitive to the amount in the bulk alloy phase (i.e., the effect saturates). These two observations indicate that the inhibiting species is metallic and that it probably forms by a dissolution/precipitation mechanism, in which the oxidized inhibitor species ($M(OH)_x^{y-}$) is reduced to the metallic state by the more electronegative aluminum.

The model for the above theory is shown schematically in Figure 10. The model proposes that, in the passive state, the surface is protected by a thin layer of metallic alloying element(s). Activation (b) occurs when the potential is positive enough ($>E_{crit}$) to cause the oxidative dissolution of M to form some dissolved species $M(OH)_x^{y-}$, thereby exposing the base aluminum. In the active state, the electrodissolution of aluminum is envisaged to occur through a layer of corrosion product (e.g., $Al(OH)_3$) whose properties are such that the current varies approximately linearly with voltage. If the potential is then displaced below (more negative than) E_{crit}, the more electropositive alloying element precipitates at the interface to again form the protective layer and hence to passivate the surface.

Assuming that the activation process is reversible and rapid, the critical activation potential (E_{crit}) should coincide roughly with the equilibrium potential for the oxidation of the alloying element(s) in

18
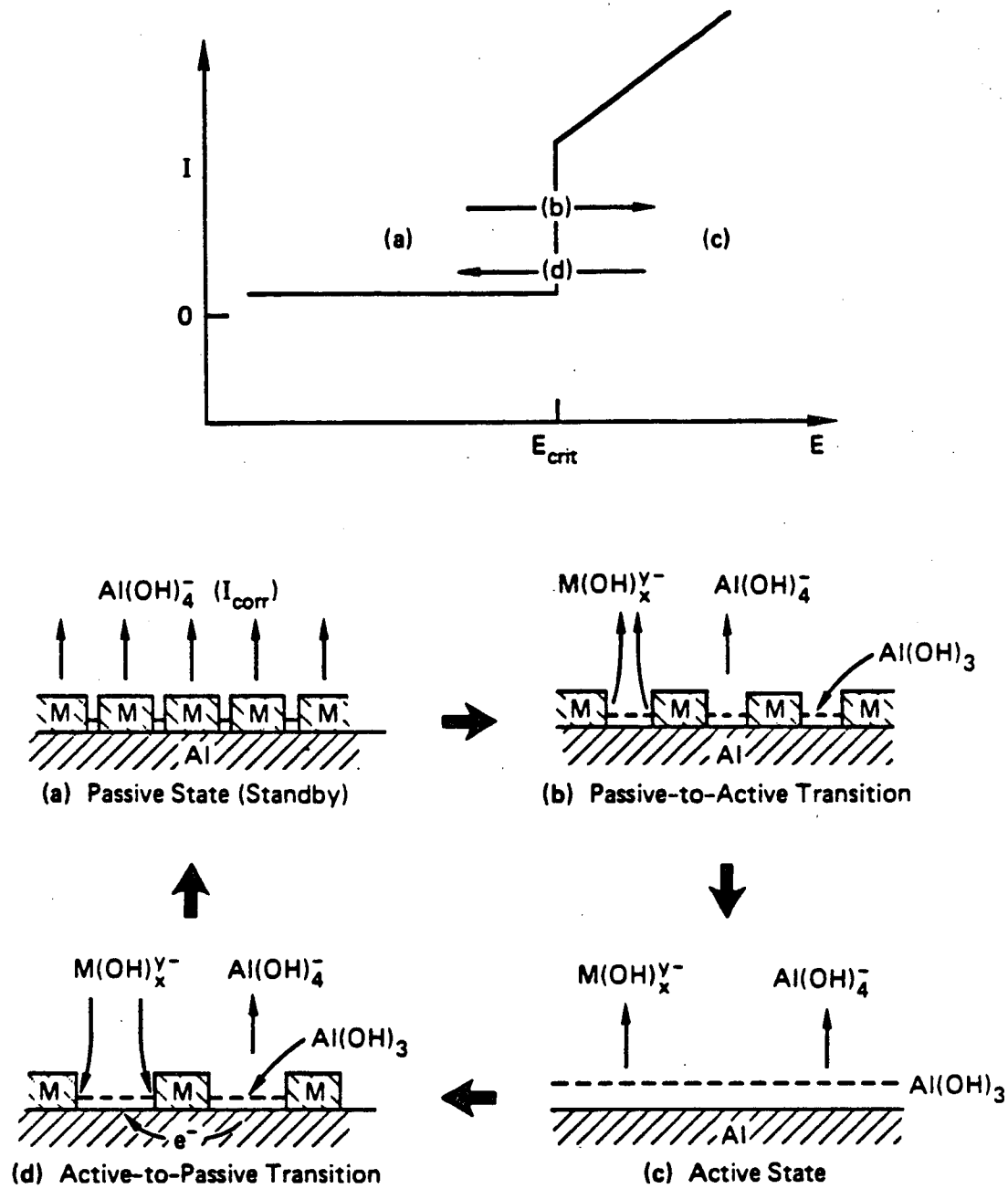
Figure 10. Schematic model of events that occur on the activation and deactivation of an aluminum alloy anode.

RA-m-320583-41

19

the concentrated hydroxide solution of interest. In the case of Alloy No. 20, the principal alloying element is gallium and, according to Pourbaix (20), the equilibrium potential for the Ga/GaO_3^{3-} couple is about -1.5 V on the Hg/HgO scale at 25°C. This potential coincides reasonably well with the potential at which activation begins (Figure 6).

III BASIS FOR PRESENT STUDIES

The work summarized above predicts that a superior aluminum anode should have the following characteristics (see Figure 9):

- A very negative critical activation potential (E_{crit}).

- A high dissolution current (I_d).

- A low standby corrosion current (I_{corr}).

Based on our present findings, E_{crit} apparently is determined by the oxidation potential of one of the alloying elements. Furthermore, this alloying element must satisfy the following conditions:

- The element must be relatively nontoxic.

- It must oxidize to form a soluble product and not passivate the aluminum surface.

- It must not poison the oxygen reduction reaction occurring at the air electrode.

- The reduction potential must be sufficiently positive that the element can be maintained in the metallic state at open circuit by aluminum and that insignificant hydrogen evolution occurs.

- The reduction potential must be sufficiently negative to yield a high power density.

Recently, we surveyed the electrochemistry of various elements to identify alloying components for activating advanced anode alloy fuels for Al/air batteries (Table 2). Of the various elements surveyed, those with equilibrium potentials lying between -1.5 V and -2 V were considered promising; the upper end (-1.5 V) being equal to that for gallium (which is now used) and the lower end (-2 V) corresponding to the most negative potential that might be achieved in a well-inhibited system without massive hydrogen evolution. Only six elements fall into this range (Table 3): B, Si, Cr, Mn, Ga, and possibly Zn.

During our previous work (10,12), ALCAN reported that an Al-Mn-Mg-In alloy (which ALCAN termed Alloy BDW) exhibited a very negative open circuit potential of approximately -1800 mV (vs Hg/HgO, 4 M KOH) and a

21

Table 2

SUMMARY OF EQUILIBRIUM ELECTRODISSOLUTION
POTENTIALS FOR POSSIBLE ALLOYING ELEMENTS

Element	Reaction		$E°(V)$*	Comments
Al	$Al + 2H_2O$	$= AlO_2^- + 4H^+ + 3e^-$	-2.5	Base metal
Be	$Be + 2H_2O$	$= BeO_2^{2-} + 4H^+ + 2e^-$	-2.8	Extremely toxic
B	$B + 3H_2O$	$= BO_3^- + 6H^+ + 5e^-$	-2.0	Nontoxic, readily available
Ti	$Ti(OH)_3$	$= HTiO_3^- + 2H^+ + e^-$	-1.1	Unlikely that Ti will form
Zr	$Zr + 3H_2O$	$= HZrO_3^- + 5H^+ + 4e^-$	-2.5	$E°$ too negative
Hf	$Hf + 3H_2O$	$= HHfO_3^- + 5H^+ + 4e^-$	?	Thermodynamics unknown
V	$V_2O_3 + 5H_2O$	$= 2VO_4 3- + 10H^+ + 4e^-$	-1.2	V not formed till -1.8
Cr	$Cr + 3H_2O$	$= CrO_3 3- + 6H^+ + 3e^-$	-1.6	Toxic
Mo	$Mo + 4H_2O$	$= MoO_4^{2-} + 8H^+ + 6e^-$	-1.2	Nontoxic
W	$W + 4H_2O$	$= WO_4^{2-} + 8H^+ + 6e^-$	-1.2	Nontoxic
Mn	$Mn + 2H_2O$	$= HMnO_2^- + 3H^+ + 2e^-$	-1.7	Nontoxic
Ga	$Ga + 3H_2O$	$= GaO_3^{3-} + 6H^+ + 3e^-$	-1.5	Most commonly used
In	$In + 2H_2O$	$= InO_2^- + 4H^+ + 3e^-$	-1.1	Commonly used
Tl	$Tl = Tl^+ + e^-$		-0.4	No known oxyanion
Si	$Si + 3H_2O$	$= SiO_3^{2-} + 6H^+ + 4e^-$	-1.8	Nontoxic
Ge	$Ge + 3H_2O$	$= GeO_3^{2-} + 6H^+ + 4e^-$	-1.3	--
Sn	$Sn + 2H_2O$	$= HSnO_2^- + 3H^+ + 2e^-$	-1.1	Commonly used
Pb	$Pb + 2H_2O$	$= HPbO_2^- + 3H^+ + 2e^-$	-0.7	Toxic
As	$As + 4H_2O$	$= AsO_4^{3-} + 8H^+ + 5e^-$	-0.9	Toxic

*Estimated from data of Pourbaix (20) for 4 M KOH at 25°C.

low corrosion rate. We later studied the electrochemical properties of Alloy BDW in 4 M KOH at 25°, 50°, and 80°C, and we showed that activation occurs by a sudden increase in the partial anodic current in a manner that is similar to that displayed in Figures 6 through 8. On thermodynamic grounds, we argued that the activating element is manganese, which is one of the candidate activators listed in Table 3. A particularly attractive feature of Alloy BDW is that it does not contain toxic alloying elements such as Tl and hence should be environmentally acceptable.

Our present work seeks to extend these studies to three other groups of alloys, one of which includes manganese as an activator. These alloys (Table 4) are as follows:

Group 1: Al-Li-In
Group 2: Al-Li-In-Bi
Group 3: Al-Mn-Mg-In

The alloys were prepared by Reynolds Aluminum Company and were kindly supplied to us by ELTECH Systems Corp.

Group 1 alloys contain small additions of lithium and indium; because of its low atomic weight and high energy content, lithium should increase the energy density of the fuel and possibly help moderate the activity of aluminum by forming sparsely soluble LiOH on the surface. Indium was added because of its efficacy as an alloying element in previous studies. Group 2 alloys are similar, except for the addition of bismuth. In our previous work, bismuth was found (Figure 2) to displace the open circuit potential to exceptionally negative values. However, neither Group 1 nor Group 2 alloys contains an activating element that meets the criteria outlined above, particularly with respect to the critical activation potential for oxidation from the metallic state lying more negative than -1.5 V.

Group 3 alloys were prepared to expand on the BDW alloy, which was found to be so promising by ALCAN and which we extensively studied in our previous program (10,12). In the present series, the relative amounts of Mn, Mg, and In are varied to determine compositional effects

23

Table 3

SUMMARY OF MOST PROMISING ACTIVATING ELEMENTS

Element	E°(V)	Toxicity	Comments
B	-2.0	Low	The most promising if the overpotential for hydrogen evolution during standby can be made very large. Power density should be high, but coulombic efficiency is likely to be low because of H_2 evolution during discharge.
Cr	-1.6	Med	To our knowledge, chromium has not been investigated as any activating element.
Mn	-1.7	Low	Manganese was thought to be beneficial because of its interaction with iron but our recent work (10,12) demonstrates that it acts as an activator. To our knowledge, no systematic work has been reported on Al-Mn alloys for Al/air batteries.
Ga	-1.5	Low?	Most commonly used element. Activation known to occur at -1.5 V and to be reversible. Standard against which other activating elements must be judged.
Si	-1.8	Low	Silicon is a common alloying element, but its effectiveness in activating aluminum anodes in alkali media is unknown.
Zn	-1.4	Low	Some work was performed on Al-Zn binary alloys previously, (13) but no systematic study of this element in ternary and quaternary alloys has been reported.

on alloy performance. However, the variations in the concentrations of these elements are neither wide enough or systematic enough to permit a quantitative analysis of synergistic effects.

The current program was not sufficiently extensive (about 3/4 man-year) to permit analysis of all the alloys listed in Table 4. Accordingly, we selected 15 alloys from the three groups for experimental evaluation (Table 5). Those selected were a compromise between our desire to investigate as many alloys as possible, and hence to explore as many individual compositional effects as feasible, and the limited resources available for this work.

Table 4

CANDIDATE ALLOYS

GROUP 1 ALLOY COMPOSITIONS (WT %)

TLI, TIN - Target Li, In compositions
LI, IN, SI, FE - Actual Li, In, Si, Fe compositions

------------------------- ELTECH ALLOY NUMBER 1 -------------------------

REYNO*	TLI	TIN	LI	IN	SI	FE
60507	0.10	0.04	0.090	0.040	0.006	0.005

------------------------- ELTECH ALLOY NUMBER 2 -------------------------

REYNO	TLI	TIN	LI	IN	SI	FE
60508	0.58	0.04	0.580	0.036	0.005	0.005

------------------------- ELTECH ALLOY NUMBER 3 -------------------------

REYNO	TLI	TIN	LI	IN	SI	FE
60509	0.10	0.20	0.033	0.200	0.006	0.004
60667	0.10	0.20	0.060	0.190	0.007	0.004

------------------------- ELTECH ALLOY NUMBER 4 -------------------------

REYNO	TLI	TIN	LI	IN	SI	FE
60510	0.58	0.20	0.430	0.210	0.005	0.005
60668	0.58	0.20	0.480	0.190	0.005	0.005

------------------------- ELTECH ALLOY NUMBER 5 -------------------------

REYNO	TLI	TIN	LI	IN	SI	FE
60511	0.00	0.12	0.000	0.110	0.006	0.005

---

*Number assigned by Reynolds Aluminum Co.

Table 4 (Continued)

GROUP 1 ALLOY COMPOSITIONS (Concluded)

TLI, TIN - Target Li, In compositions
LI, IN, SI, FE - Actual Li, In, Si, Fe compositions

------------------------ ELTECH ALLOY NUMBER 6 ------------------------

REYNO	TLI	TIN	LI	IN	SI	FE
60512	0.68	0.12	0.700	0.110	0.005	0.005

------------------------ ELTECH ALLOY NUMBER 7 ------------------------

REYNO	TLI	TIN	LI	IN	SI	FE
60513	0.34	0.00	0.310	0.006	0.005	0.005

------------------------ ELTECH ALLOY NUMBER 8 ------------------------

REYNO	TLI	TIN	LI	IN	SI	FE
60514	0.34	0.23	0.160	0.220	0.005	0.004
60669	0.34	0.23	0.230	0.280	0.005	0.005

------------------------ ELTECH ALLOY NUMBER 9 ------------------------

REYNO	TLI	TIN	LI	IN	SI	FE
60515	0.34	0.12	0.240	0.110	0.005	0.005
60670	0.34	0.12	0.280	0.110	0.006	0.005

Table 4 (Continued)

GROUP 2 ALLOY COMPOSITIONS   (Wt %)

TLI, TIN, TBI = Target Li, In, Bi compositions
LI, IN, BI, SI, FE = Actual Li, In, Bi, Si, Fe compositions

-------------------------- ELTECH ALLOY NUMBER 10 ------------------------

REYNO	TLI	TIN	TBI	LI	IN	BI	SI	FE
60516	0.10	0.04	0.04	0.065	0.042	0.030	0.006	0.005

-------------------------- ELTECH ALLOY NUMBER 11 ------------------------

REYNO	TLI	TIN	TBI	LI	IN	BI	SI	FE
60655	0.39	0.04	0.04	0.350	0.035	0.018	0.011	0.006

-------------------------- ELTECH ALLOY NUMBER 12 ------------------------

REYNO	TLI	TIN	TBI	LI	IN	BI	SI	FE
60518	0.10	0.15	0.04	0.003	0.140	0.040	0.008	0.005
60519	0.10	0.15	0.04	0.140	0.130	0.040	0.009	0.005

-------------------------- ELTECH ALLOY NUMBER 13 ------------------------

REYNO	TLI	TIN	TBI	LI	IN	BI	SI	FE
60663	0.39	0.15	0.04	0.300	0.150	0.013	0.007	0.005

-------------------------- ELTECH ALLOY NUMBER 14 ------------------------

REYNO	TLI	TIN	TBI	LI	IN	BI	SI	FE
60656	0.10	0.040	0.15	0.082	0.035	0.120	0.006	0.005

-------------------------- ELTECH ALLOY NUMBER 15 ------------------------

REYNO	TLI	TIN	TBI	LI	IN	BI	SI	FE
60657	0.39	0.04	0.15	0.230	0.033	0.022	0.005	0.005

Table 4 (Continued)

GROUP 2 ALLOY COMPOSITIONS (Continued)

---------------------- ELTECH ALLOY NUMBER 16 ----------------------

REYNO	TLI	TIN	TBI	LI	IN	BI	SI	FE
60522	0.10	0.15	0.15	0.009	0.110	0.120	0.005	0.005
60664	0.10	0.15	0.15	0.063	0.140	0.110	0.005	0.005

---------------------- ELTECH ALLOY NUMBER 17 ----------------------

REYNO	TLI	TIN	TBI	LI	IN	BI	SI	FE
60658	0.39	0.15	0.15	0.290	0.150	0.018	0.006	0.005

---------------------- ELTECH ALLOY NUMBER 18 ----------------------

REYNO	TLI	TIN	TBI	LI	IN	BI	SI	FE
60524	0.00	0.10	0.10	0.000	0.080	0.090	0.004	0.005

---------------------- ELTECH ALLOY NUMBER 19 ----------------------

REYNO	TLI	TIN	TBI	LI	IN	BI	SI	FE
60659	0.49	0.10	0.10	0.350	0.094	0.014	0.006	0.004

---------------------- ELTECH ALLOY NUMBER 20 ----------------------

REYNO	TLI	TIN	TBI	LI	IN	BI	SI	FE
60660	0.25	0.00	0.10	0.150	0.000	0.047	0.007	0.004

---------------------- ELTECH ALLOY NUMBER 21 ----------------------

REYNO	TLI	TIN	TBI	LI	IN	BI	SI	FE
60527	0.25	0.19	0.10	0.042	0.190	0.080	0.005	0.006
60665	0.25	0.19	0.10	0.180	0.170	0.065	0.005	0.005

Table 4 (Continued)

GROUP 2 ALLOY COMPOSITIONS (Concluded)

---------------------- ELTECH ALLOY NUMBER 22 ----------------------

REYNO	TLI	TIN	TBI	LI	IN	BI	SI	FE
60528	0.25	0.10	0.00	0.210	0.100	0.000	0.004	0.005
60666	0.25	0.10	0.00	0.180	0.090	0.012	0.005	0.005

---------------------- ELTECH ALLOY NUMBER 23 ----------------------

REYNO	TLI	TIN	TBI	LI	IN	BI	SI	FE
60661	0.25	0.10	0.19	0.140	0.096	0.052	0.006	0.005

---------------------- ELTECH ALLOY NUMBER 24 ----------------------

REYNO	TLI	TIN	TBI	LI	IN	BI	SI	FE
60662	0.25	0.10	0.10	0.160	0.090	0.033	0.005	0.006

Table 4 (Continued)

GROUP 3 ALLOY COMPOSITIONS (Wt %)

TMN, TMG, TIN — Target Mn, Mg, In compositions
MN, MG, IN, SI, FE — Actual Mn, Mg, In, Si, Fe compositions

---------------------- ELTECH ALLOY NUMBER 25 ----------------------

REYNO	TMN	TMG	TIN	MN	MG	IN	SI	FE
60531	0.10	0.22	0.07	0.12	0.24	0.076	0.007	0.005

---------------------- ELTECH ALLOY NUMBER 26 ----------------------

REYNO	TMN	TMG	TIN	MN	MG	IN	SI	FE
60532	0.15	0.22	0.07	0.16	0.24	0.078	0.008	0.005

---------------------- ELTECH ALLOY NUMBER 27 ----------------------

REYNO	TMN	TMG	TIN	MN	MG	IN	SI	FE
60533	0.10	0.80	0.07	0.11	0.81	0.064	0.008	0.005

---------------------- ELTECH ALLOY NUMBER 28 ----------------------

REYNO	TMN	TMG	TIN	MN	MG	IN	SI	FE
60534	0.15	0.80	0.07	0.16	0.79	0.066	0.009	0.005

---------------------- ELTECH ALLOY NUMBER 29 ----------------------

REYNO	TMN	TMG	TIN	MN	MG	IN	SI	FE
60535	0.10	0.22	0.20	0.11	0.23	0.180	0.007	0.005

---------------------- ELTECH ALLOY NUMBER 30 ----------------------

REYNO	TMN	TMG	TIN	MN	MG	IN	SI	FE
60536	0.15	0.22	0.20	0.17	0.22	0.180	0.009	0.005

Table 4 (Continued)

GROUP 3 ALLOY COMPOSITIONS (Continued)

---------------------- ELTECH ALLOY NUMBER 31 -----------------------

REYNO	TMN	TMG	TIN	MN	MG	IN	SI	FE
60537	0.10	0.80	0.20	0.12	0.79	0.180	0.008	0.005

---------------------- ELTECH ALLOY NUMBER 32 -----------------------

REYNO	TMN	TMG	TIN	MN	MG	IN	SI	FE
60538	0.15	0.80	0.20	0.17	0.76	0.180	0.010	0.005

---------------------- ELTECH ALLOY NUMBER 33 -----------------------

REYNO	TMN	TMG	TIN	MN	MG	IN	SI	FE
60539	0.08	0.51	0.14	0.10	0.48	0.130	0.008	0.004

---------------------- ELTECH ALLOY NUMBER 34 -----------------------

REYNO	TMN	TMG	TIN	MN	MG	IN	SI	FE
60540	0.17	0.51	0.14	0.20	0.47	0.130	0.008	0.005

---------------------- ELTECH ALLOY NUMBER 35 -----------------------

REYNO	TMN	TMG	TIN	MN	MG	IN	SI	FE
60541	0.13	0.02	0.14	0.16	0.02	0.120	0.006	0.005

---------------------- ELTECH ALLOY NUMBER 36 -----------------------

REYNO	TMN	TMG	TIN	MN	MG	IN	SI	FE
60542	0.13	1.00	0.14	0.17	1.00	0.120	0.015	0.006

Table 4 (Concluded)

GROUP 3 ALLOY COMPOSITIONS (Concluded)

---------------------- ELTECH ALLOY NUMBER 37 ----------------------

REYNO	TMN	TMG	TIN	MN	MG	IN	SI	FE
60543	0.13	0.51	0.03	0.13	0.52	0.066	0.007	0.005

---------------------- ELTECH ALLOY NUMBER 38 ----------------------

REYNO	TMN	TMG	TIN	MN	MG	IN	SI	FE
60544	0.13	0.51	0.24	0.14	0.51	0.230	0.016	0.006

---------------------- ELTECH ALLOY NUMBER 39 ----------------------

REYNO	TMN	TMG	TIN	MN	MG	IN	SI	FE
60545	0.13	0.51	0.14	0.13	0.52	0.160	0.008	0.005

Table 5

ALLOYS EMPLOYED IN EXPERIMENTAL STUDIES

Reynold/s Alloy No.	Composition (Wt %)				

Group 1 (Al-Li-In)

	Li	In	Si	Fe
60511 (Eltech 5)	0.000	0.110	0.006	0.005
60512 (Eltech 6)	0.700	0.110	0.005	0.005
60513 (Eltech 7)	0.310	0.006	0.005	0.005

Group 2 (Li-In-Bi)

	Li	In	Bi	Si	Fe
60518 (Eltech 12)	0.003	0.140	0.040	0.008	0.005
60519 (Eltech 12)	0.140	0.130	0.040	0.009	0.005
60522 (Eltech 16)	0.009	0.110	0.120	0.005	0.005
60524 (Eltech 18)	0.000	0.080	0.090	0.004	0.005
60660 (Eltech 20)	0.150	0.000	0.047	0.007	0.004
60664 (Eltech 16)	0.063	0.140	0.110	0.005	0.005

Group 3 (Al-Mn-Mg-In)

	Mn	Mg	In	Si	Fe
60531 (Eltech 25)	0.12	0.24	0.076	0.007	0.005
60533 (Eltech 27)	0.11	0.81	0.064	0.008	0.005
60535 (Eltech 29)	0.11	0.23	0.180	0.007	0.005
60537 (Eltech 31)	0.12	0.79	0.180	0.008	0.005
60539 (Eltech 33)	0.10	0.48	0.130	0.008	0.004
60540 (ELTECH 34)	0.20	0.47	0.130	0.008	0.005

IV EXPERIMENTAL PROCEDURES

A. Apparatus

The electrochemical behavior of each alloy in 4 M KOH at 50°C was studied using the flow loop previously described (9,12). This loop contains a reservoir, a positive-displacement circulation pump, a flow meter, and the test cell. The reservoir is immersed into a constant-temperature water bath, whose temperature is set to yield a value of 50°C at the entrance to the test cell, as measured by a calibrated thermocouple. The solution in the reservoir is continuously sparged with nitrogen to prevent the buildup of hydrogen in the system. This step is important because the porous collector electrode, which is located downstream from the aluminum working electrode, is calibrated for hydrogen oxidation under carefully controlled conditions of solution flow rate and nitrogen sparging of the reservoir (9).

B. Delineation of Anodic and Cathodic Partial Reactions

The cathodic and anodic partial currents were delineated using a porous platinized nickel electrode downstream of the aluminum alloy specimen in a flowing system to collect the evolved hydrogen. We have previously described (9,12) the calibration of this system, and we have shown that, provided the hydrodynamic conditions are maintained reproducible, cathodic currents may be determined to better than ± 0.1 mA or to about ± 0.1% of the maximum current that will be sampled in this study.

C. AC Impedance Spectroscopy

Impedance spectra were measured using a computer-controlled SOLARTRON 1250 Frequency Response Analyzer. The impedance data are tested on-line for their validity using Kramers-Kronig (K-K) transforms, as described previously (12,21,22). To our knowledge, this on-line K-K analysis capability is unique, but we have shown previously that it is essential if accurate impedance data are to be obtained for inherently unstable (rapidly corroding) systems, such as aluminum alloys in alkali solutions.

D. Solutions

All solutions were prepared using Analytical Reagent grade KOH and deionized water.

V RESULTS AND DISCUSSION

Delineated current/voltage curves for the 15 alloys studied in this program are shown in the figures in this section. Each plot displays the observed or total current (iT), the alloy dissolution current (iA), and the hydrogen evolution current (iH) as a function of potential over the range of accessible current (approx. -400 mA/cm^2 to 500 mA/cm^2). Table 6 summarizes characteristic data for each alloy, including the open circuit potential (E_{OCP}), corrosion current (i_{corr}), and the critical activation potential (E_{crit}, if any). The corrosion rates listed in parentheses were measured from the hydrogen evolution rate under open circuit conditions.

A. Group 1 Alloys

Figures 11 through 13 show current/voltage curves for the partial anodic (iA) and partial cathodic (iH) processes, as well as the total current versus potential for Alloys 60511 to 60513 in 4 M KOH at 50°C. In all three cases, the observed current (iT) and the currents for the delineated partial processes are large, particularly for Alloys 60511 and 60512. In these instances, the current/voltage curves are very steep, with the open circuit potentials lying within the range -1.66 to -1.77 V (vs Hg/HgO, 4 M KOH). Furthermore, the corrosion currents (iA at E_{OCP}) are exceptionally high (340 mA/cm^2 and 270 mA/cm^2 for Alloys 60511 and 60512, respectively), indicating that these alloys are unsuitable as fuels for aluminum/air batteries.

In the case of Alloy 60513, high anodic (iA) and cathodic (iH) currents are also observed at potentials in the neighborhood of the open circuit value (i_{corr} = 260 mA/cm^2), but at higher potentials the surface passivates, resulting in a decrease in the dissolution current and a virtual inhibition of hydrogen evolution. At still higher (more positive) potentials, the total (iT) and alloy dissolution (iA) currents increase nearly linearly with voltage, but at a rate that is much less than that for pure aluminum (Figure 4). This alloy differs from the other two in this group by being virtually devoid of indium and containing only a modest amount of lithium (0.31%).
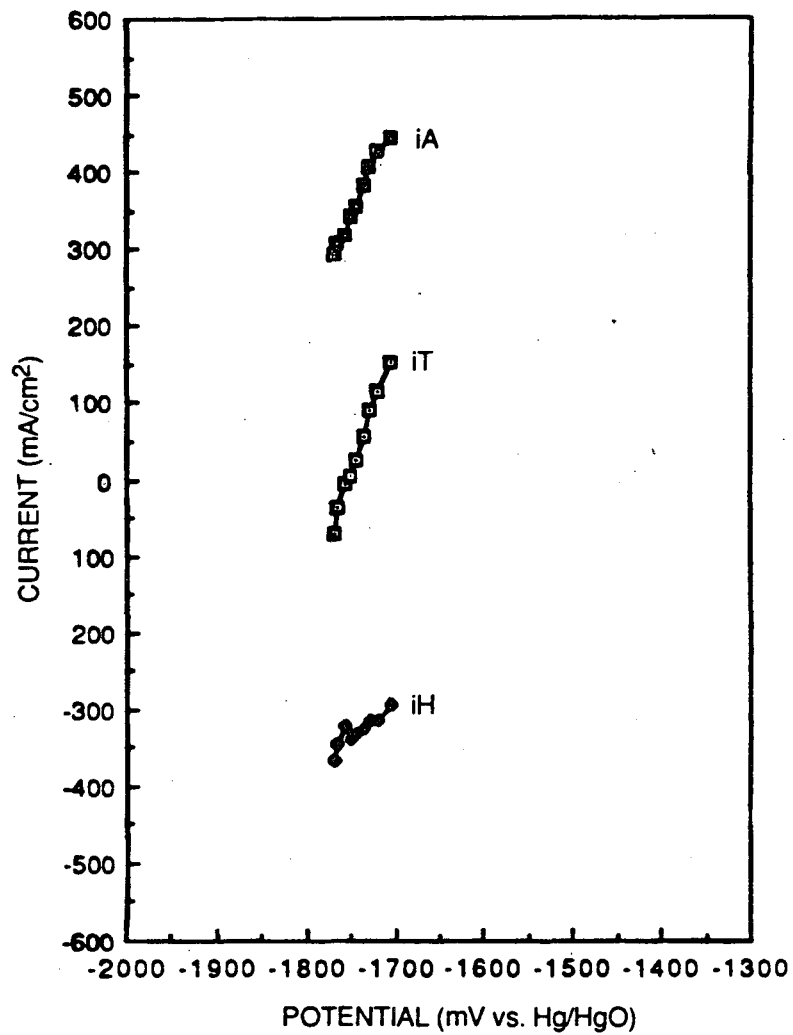
RA-3357-1

Figure 11. The total current (iT) and delineated anodic (iA) and
cathodic (iH) current/voltage curves for Alloy 60511
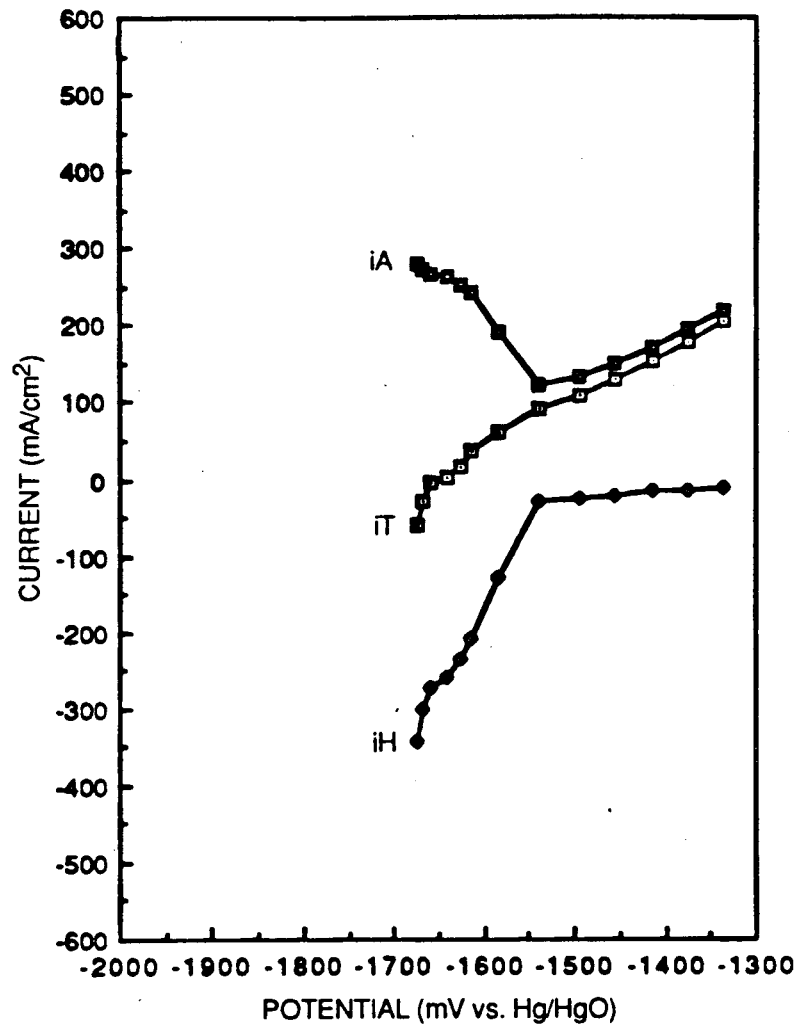in 4 M KOH at 50°C.

Potential corrected for IR_s drop with $R_s = 0.6 \ \Omega$.

38
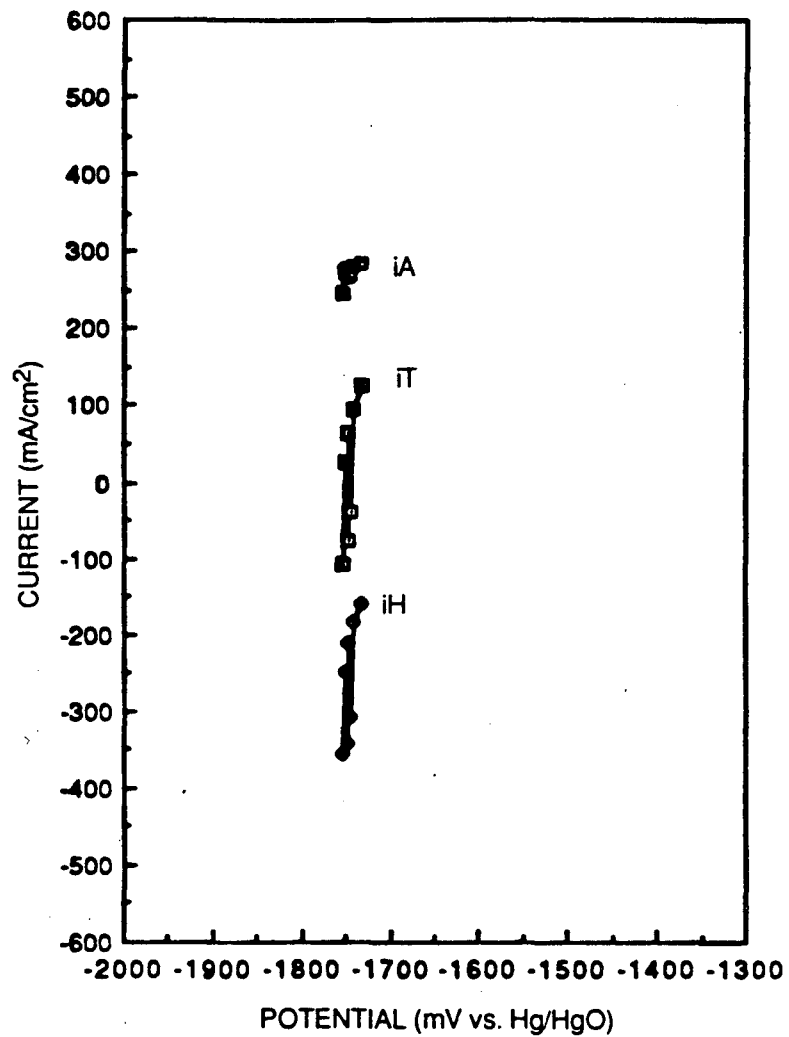
Figure 12. The total current (iT) and delineated anodic (iA) and cathodic (iH) current/voltage curves for Alloy 60512 in 4 M KOH at 50°C.

Potential corrected for IR_s drop with $R_s = 0.6\ \Omega$.

Figure 13. The total current (iT) and delineated anodic (iA) and cathodic (iH) current/voltage curves for Alloy 60513 in 4 M KOH at 50°C.

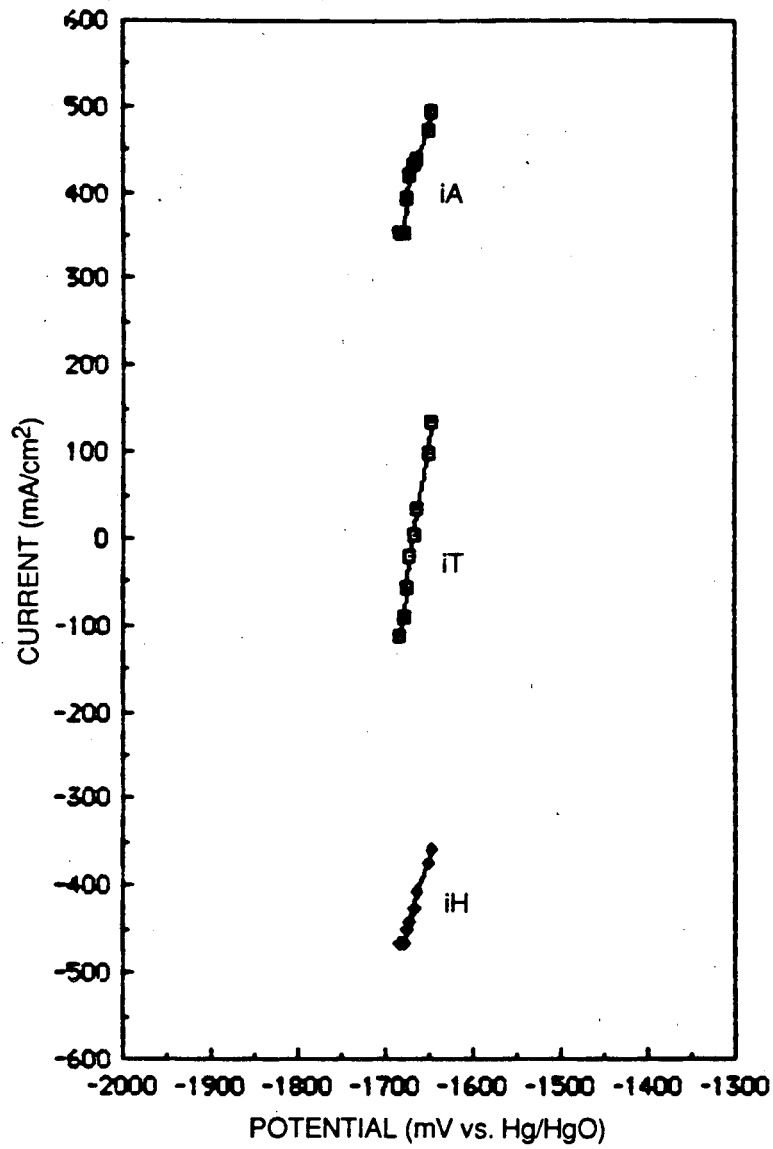Potential corrected for IR_s drop with $R_S = 0.6\ \Omega$.

The fact that alloys containing large amounts of indium have large corrosion rates is consistent with the data plotted in Figure 1, assuming that the alloy behaves essentially as a binary system. According to the data in Figure 1, the indium-containing alloys should exhibit corrosion currents which are about three times higher than for pure aluminum; this correlates well with the observed corrosion currents for Al ($\sim$120 mA/cm^2, Figure 4), Alloy 60511 ($\sim$ 340 mA/cm^2), and Alloy 60512 ($\sim$ 270 mA/cm^2). A similar ratio is also observed for Alloy 60513, even though this alloy contains little indium. Apparently, lithium has a similar effect of increasing i_{corr}.

The origin of the passivation phenomenon in the case of Alloy 60513 is unclear, but presumably it is related to the presence of lithium and the absence of indium in the alloy. However, in this case, any synergistic interaction between lithium and indium is apparently detrimental because, when both elements are present (Alloy 60512), the surface does not passivate. In any case, the corrosion currents are so high that none of the alloys investigated from this group could be considered as candidate fuels for aluminum/air batteries.

B. Group 2 Alloys

Because Group 2 alloys contain lithium, indium, and bismuth, any differences between these alloys and those of Group 1 might be attributed to the presence of Bi. However, the current/voltage curves for the Group 2 alloys, shown in Figures 14 through 20, indicate that bismuth in fact exerts very little effect on the electrochemical behavior of the alloys, with the apparent exceptions of Alloy 60522 (Figure 17) and Alloy 60660 (Figure 19).

For Alloy 60522, the hydrogen evolution current is found to increase as the potential is moved in the positive direction. Clearly, this effect is opposite to that expected from simple Butler-Volmer kinetics and must be due to changes in surface coverage of some catalytic species. However, this behavior was not reproducible, as shown by the data in Figure 16 for ostensibly an identical experiment. This latter experiment indicates normal behavior.
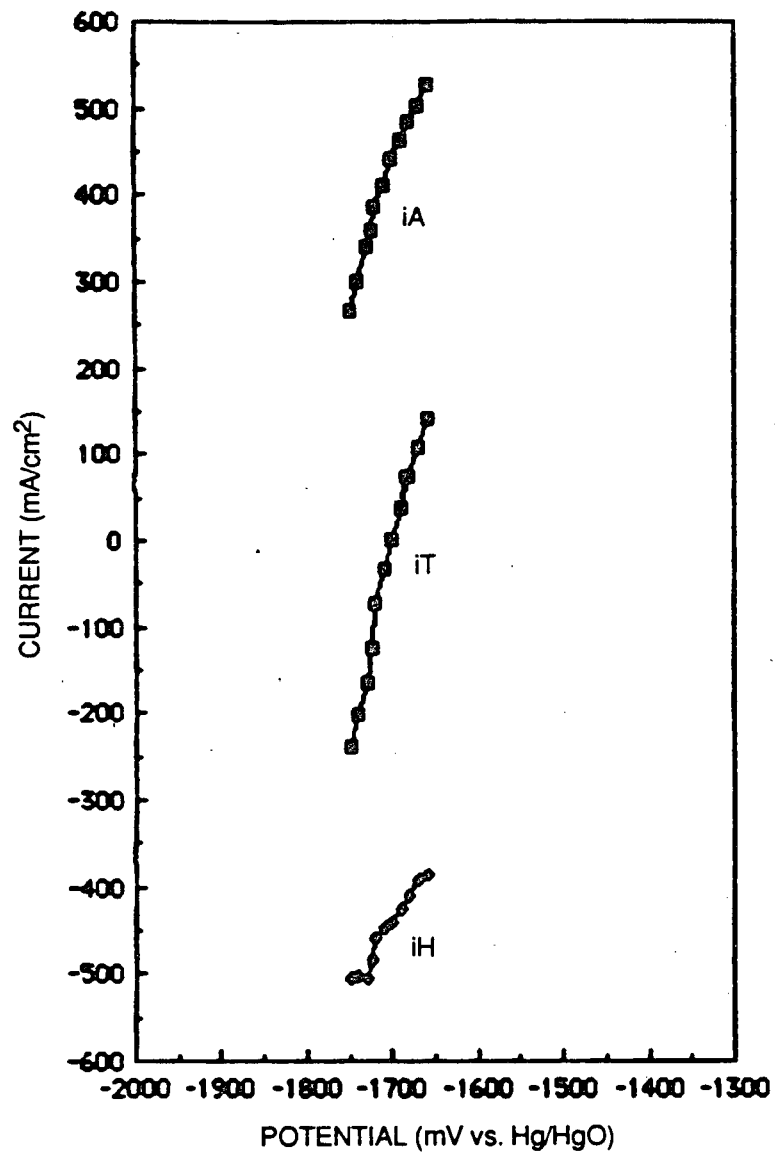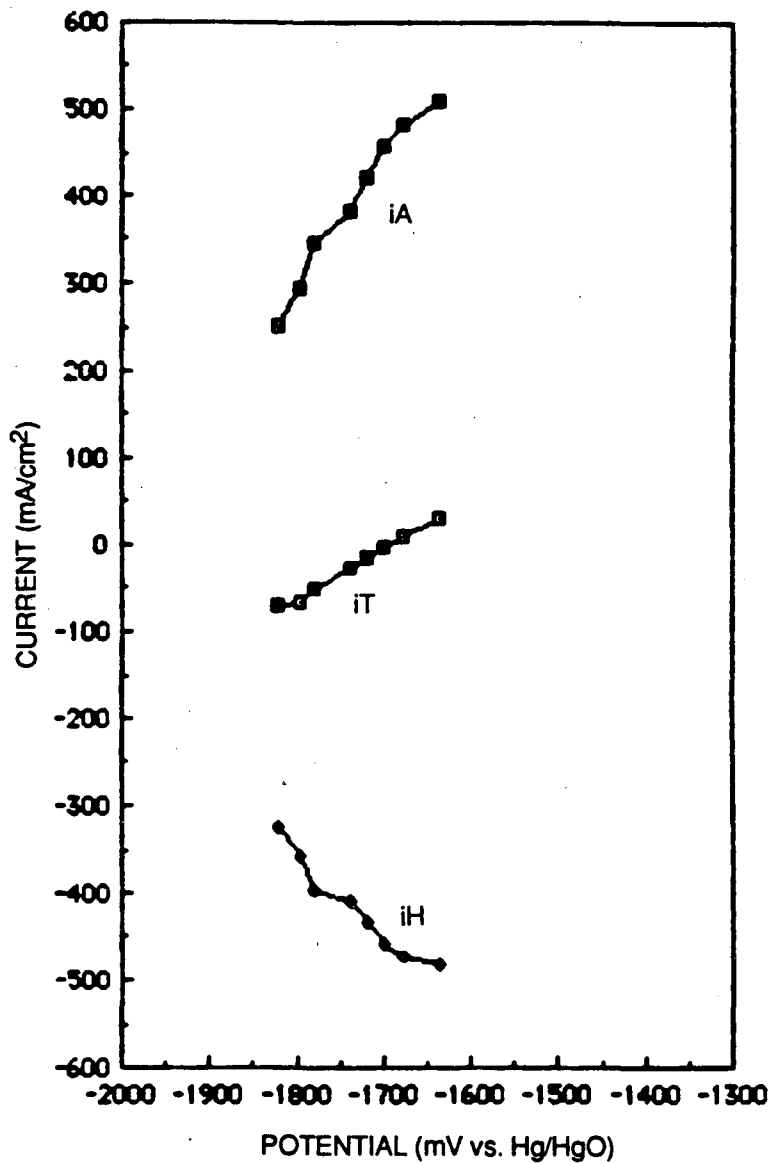
41

Figure 14. Steady state polarization curves for Alloy 60518 in 4 M KOH, 50°C, showing the total current (iT) and both anodic (iA) and cathodic (iH) partial currents.

Potential corrected for IR_s drop with $R_s = 0.6\ \Omega$.
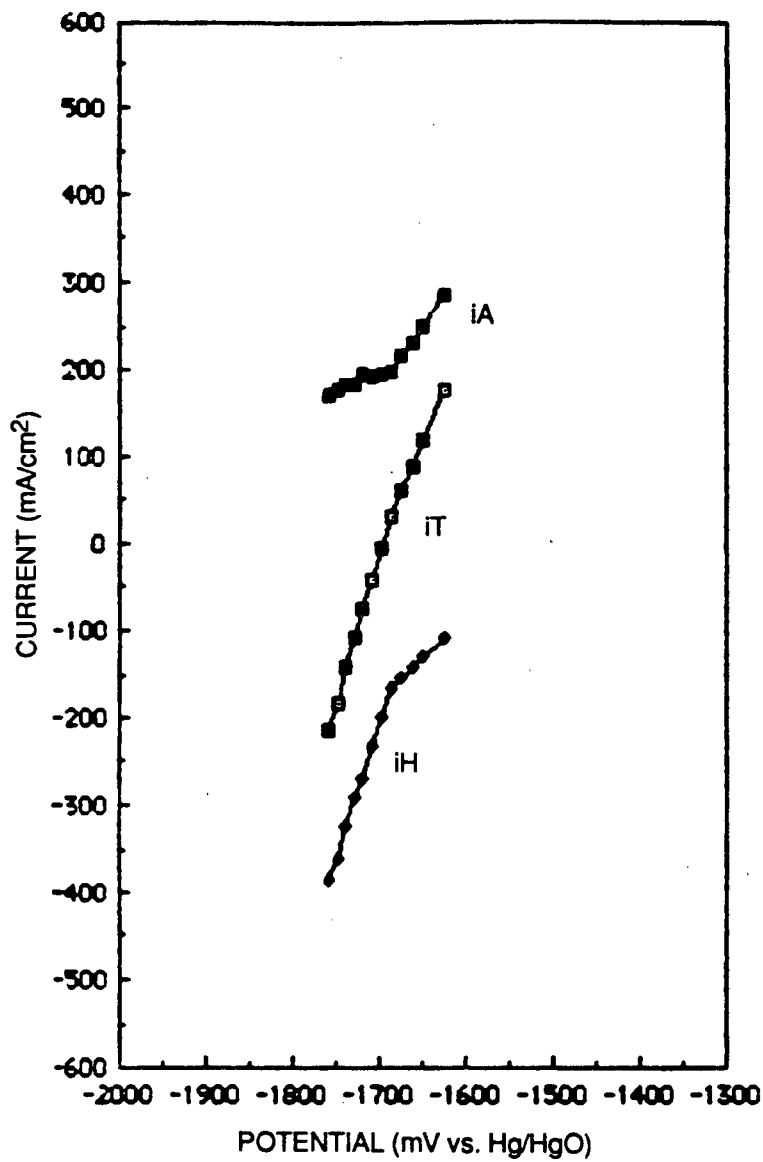
RA-3357-5

Figure 15.   Steady state polarization curves for Alloy 60519 in
4 M KOH, 50°C, showing the total current (iT) and
both anodic (iA) and cathodic (iH) partial currents.

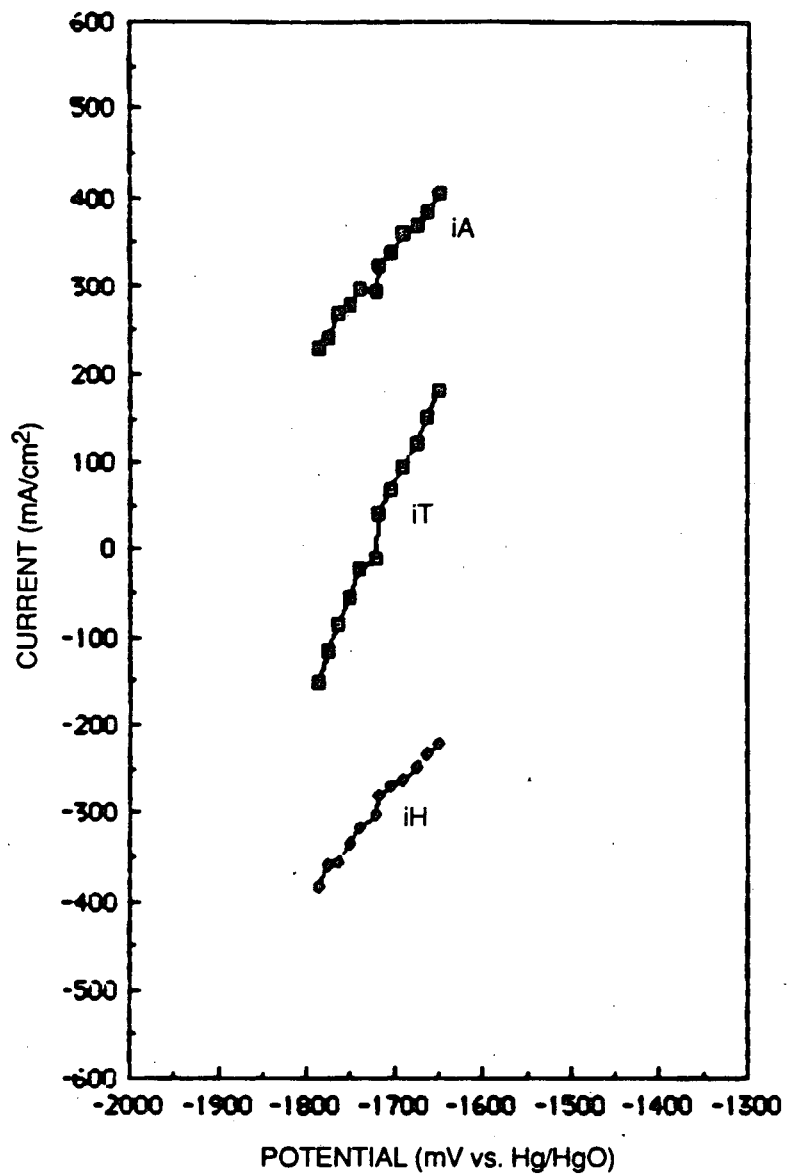Potential corrected for IR_s drop with R_s = 0.6 Ω.

43

RA-3357-6

Figure 16. Steady state polarization curves for Alloy 60522 in
4 M KOH, 50°C, showing the total (iT) current and
both anodic (iA) and cathodic (iH) partial currents.

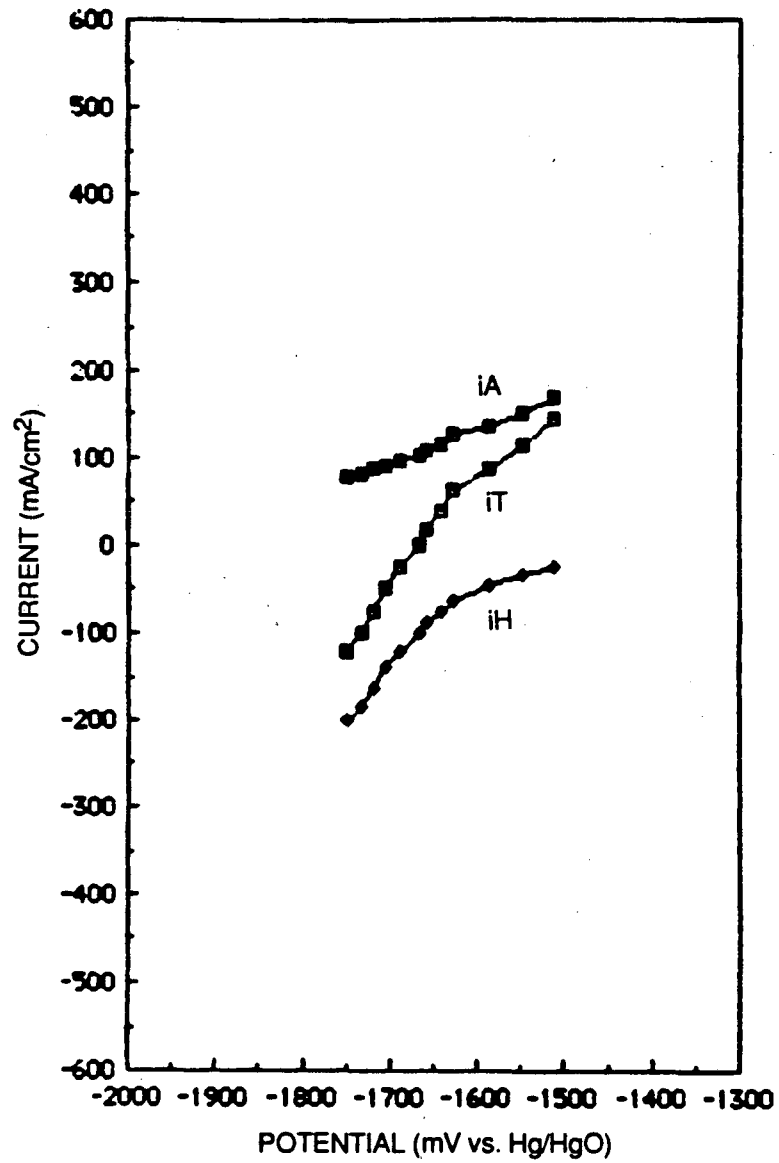Potential corrected for IR_s drop with R_s = 0.6 Ω.

44

RA-3357-7

Figure 17. Steady state polarization curves for Alloy 60522 in
4 M KOH, 50°C, showing the total (iT) current and
both anodic (iA) and cathodic (iH) partial currents.

Potential corrected for IR_s drop with R_s = 0.6 Ω.

45

RA-3357-8
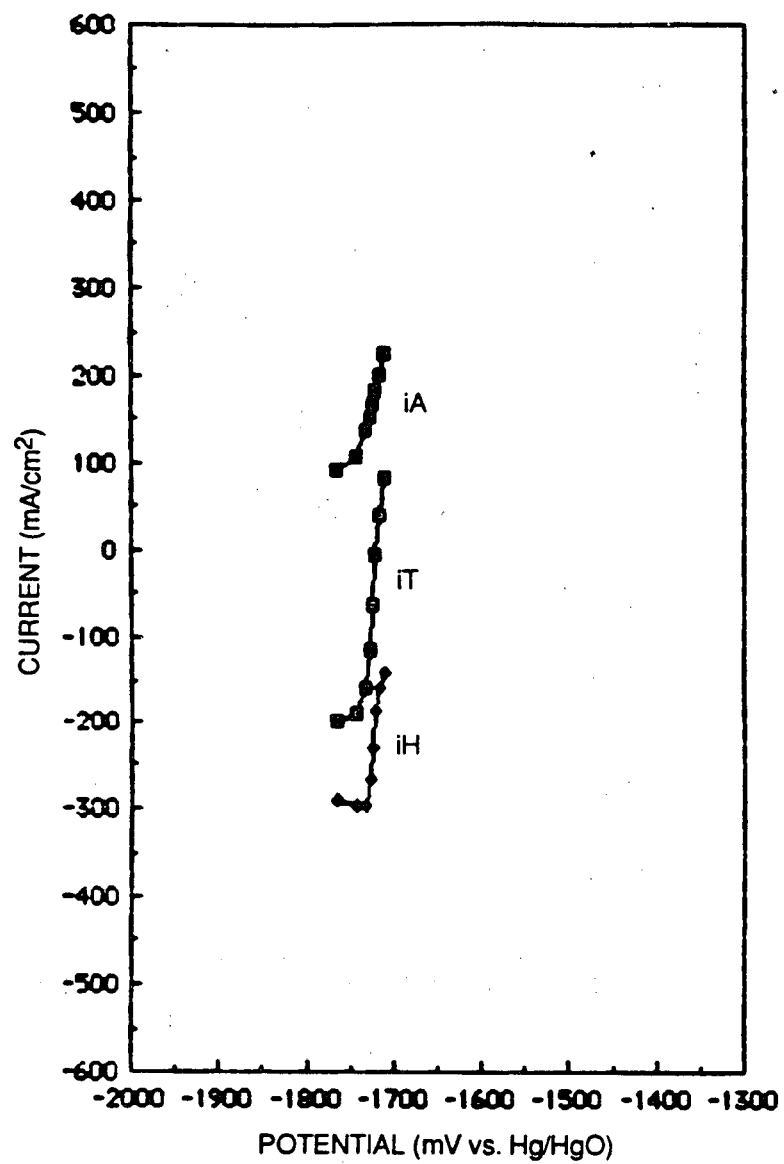
Figure 18. Steady state polarization curves for Alloy 60524 in
4 M KOH, 50°C, showing the total (iT) current and
both anodic (iA) and cathodic (iH) partial currents.

Potential corrected for IR_s drop with R_s = 0.6 Ω.

46

RA-3357-9

Figure 19. Steady state polarization curves for Alloy 60660 in 4 M KOH, 50°C, showing the total (iT) current and both anodic (iA) and cathodic (iH) partial currents.

Potential corrected for IR_s drop with $R_s = 0.6\ \Omega$.

47

RA-3357-10

Figure 20. Steady state polarization curves for Alloy 60664 in
4 M KOH, 50°C, showing the total (iT) current and
both anodic (iA) and cathodic (iH) partial currents.

Potential corrected for IR_s drop with $R_s = 0.6\ \Omega$.

Alloy 60660, which contains 0.15% Li + 0.047% Bi (zero indium), exhibits much lower currents than the other alloys at similar potentials. In this case, the corrosion current is similar to that of pure aluminum in the same environment. Furthermore, the anodic partial current is much less potential-dependent than for the other alloys, again indicating that the presence of indium in these alloys is detrimental, as it is in pure aluminum (Figure 4). Note, however, that the synergistic effects are highly specific to the particular alloy system under consideration. For example, in the presence of gallium and perhaps thallium, indium is found to be beneficial in reducing the open circuit corrosion rate (8,10).

Although bismuth is found to shift the open circuit potential in the negative direction in the binary Al-Bi system (Figure 2), the opposite appears to occur in the quaternary Al-Li-In-Bi alloys (Table 6). However, the shift is much smaller than for the binary alloys, so any beneficial effect that bismuth has on the open circuit properties is not significant in the practical sense.

As found for the alloys of Group 1, the open circuit corrosion rates for alloys of Group 2 are far too high for these materials to be considered as candidate fuels for aluminum/air batteries (see data in Table 7).

C. Group 3 Alloys

Potentially, the most suitable alloy fuels are expected to be members of Group 3 because of their general similarity to Alloy BDW (Al-1Mg-0.1In-0.2Mn); see Refs. (10) and (12), and Table 7. This expectation is borne out by the present work (compare Figures 21 through 26 with Figure 27), to the extent that these alloys not only exhibit an activation phenomenon at ~ -1.8 V (vs Hg/HgO, 4 M KOH), due to the oxidative dissolution of manganese from the surface (compare this potential with the equilibrium potential of -1.7 V for the $HMnO_2^-/Mn$ couple in 4 M KOH at 25°C listed in Table 2[*], but they also passivate at

---

[*]Note that the equilibrium potential becomes more negative with increasing temperature and that a value of -1.8 V is considered to be reasonable at 50°C.

Table 6

CHARACTERISTIC DATA FOR ALUMINUM ALLOYS IN 4 M KOH AT 25°C

Alloy	E_{OCP}* (V vs Hg/HgO)	i_{corr} (mA/cm^2)	E_{crit} (V vs Hg/HgO)	Comments
		Group 1		
60511	-1.77	340 (320)[+]	--	Alloys do not activate because neither alloying element oxidizes within the potential range of interest. Very high corrosion rates are observed.
60512	-1.75	270 (285)	--	
60513	-1.66	260 (261)	--	
		Group 2		
60518	-1.66	440 (428)	--	Very high corrosion rates are observed for this group of alloys. No activation phenomenon is noted because of the lack of an alloying element that oxidizes to form a soluble product within the potential range of interest.
60519	-1.70	200 (195)	--	
60522	-1.70	450 (444)	--	
60524	-1.72	310 (297)	--	
60660	-1.68	100 (102)	--	
60664	-1.71	200 (190)	--	

*Defined here as the potential at which the total current (iT) is zero.
[+]Values in parentheses were measured under open circuit conditions.

Table 6 (Concluded

Alloy	E_{OCP}* (V vs Hg/HgO)	i_{corr} (mA/cm^2)	E_{crit} (V vs Hg/HgO)	Comments
		Group 3		
60531	-1.80	80 (76)	-1.82	Alloys contain Mn as
60533	-1.80	150 (148)	-1.83	the activating ele-
60535	-1.79	200 (143)	-1.80	ment, and the crit-
60537	-1.78	50 (52)	-1.80	ical potential coin-
60539	-1.79	20 (50)	-1.79	cides with that for
60540	-1.80	40 (95)	-1.80	Alloy BDW, possibly
BDW	-1.81	5.6	-1.80	because of thermal processing of the latter.

*Defined here as the potential at which the total current (iT) is zero.

51

Table 7

KINETIC PARAMETERS FOR HYDROGEN EVOLUTION (i_{corr}, i_o)
AT THE CORROSION POTENTIAL (E_{corr}) AND EQUILIBRIUM
POTENTIAL ($E_\bullet$). DATA TAKEN FROM Ref (10)

Alloy	E_{corr} (V vs Hg/HgO)	i_{corr} (mA/cm^2)	$E_\bullet$ [a] (V vs Hg/HgO)	i_o [b] (mA/cm^2)	b_H [c] (mV/decade)
			T = 25°C		
Al	-1.675	25.1	-0.926	0.19	350
16	-1.640	15.8	-0.926	0.03	260
20	-1.600	2.5	-0.926	0.01	280
21	-1.660	1.4	-0.926	6×10^{-5}	160
BDW	-1.778	2.1	-0.926	4×10^{-6}	150
IN-GA	-1.650	1.8	-0.926	3×10^{-4}	190
134	-1.377	50.5	-0.926	8.5	170
			T = 50°C		
Al	-1.751	117 (92.0)[d]	-0.924	1.8	460
16	-1.680	34.6 (9.1)	-0.924	0.04	250
20	-1.560	1.9 (7.3)	-0.924	0.01	250
21	-1.640	4.6 (8.6)	-0.924	1×10^4	180
BDW	-1.800	5	-0.924	3×10^{-7}	120
IN-GA	-1.710	19.5	-0.924	4×10^{-4}	170
134	-1.790	6	-0.924	2×10^{-6}	130
			T = 80°C		
Al	-1.728	174	-0.917	4.6	510
16	--	--	-0.917	--	--
20	-1.555	25.1	-0.917	0.08	240
21	-1.668	15.8	-0.917	9×10^{-4}	180
BDW	-1.820	43.6	-0.917	3×10^{-4}	160
IN-GA	-1.715	181.9	-0.917	0.21	270
134	-1.790	79.4	-0.917	6×10^{-2}	280

[a] Equilibirum potential for the hydrogen electrode reaction.
[b] Exchange current density for hydrogen evolution.
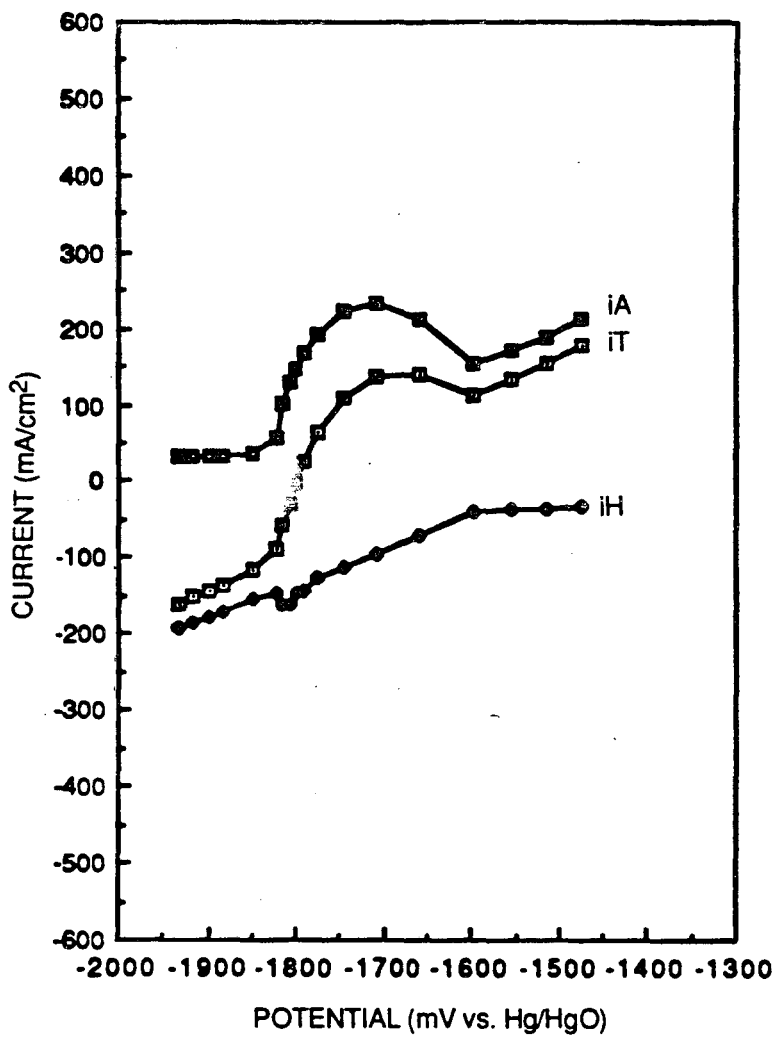[c] Tafel constant for hydrogen evolution.
[d] Calculated from weight loss data reported in Ref. (8) using Eq. (2).
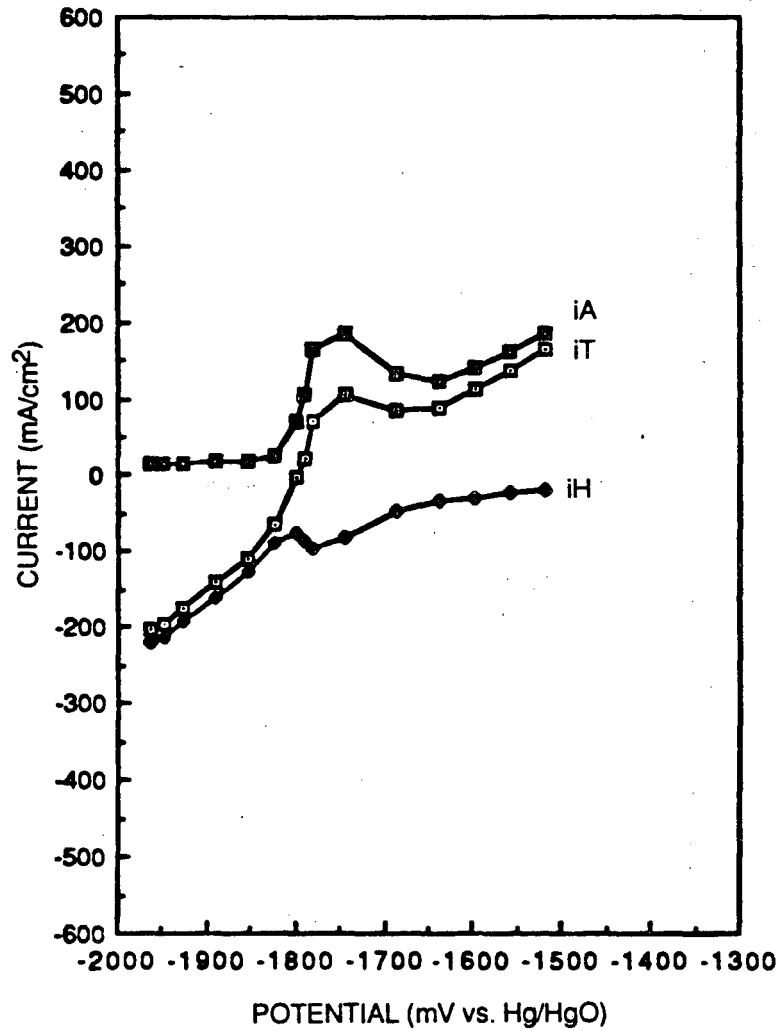
RA-3357-11

Figure 21. The total (iT) current and delineated anodic (iA) and cathodic (iH) current/voltage curves for Alloy 60531 in 4 M KOH at 50°C.
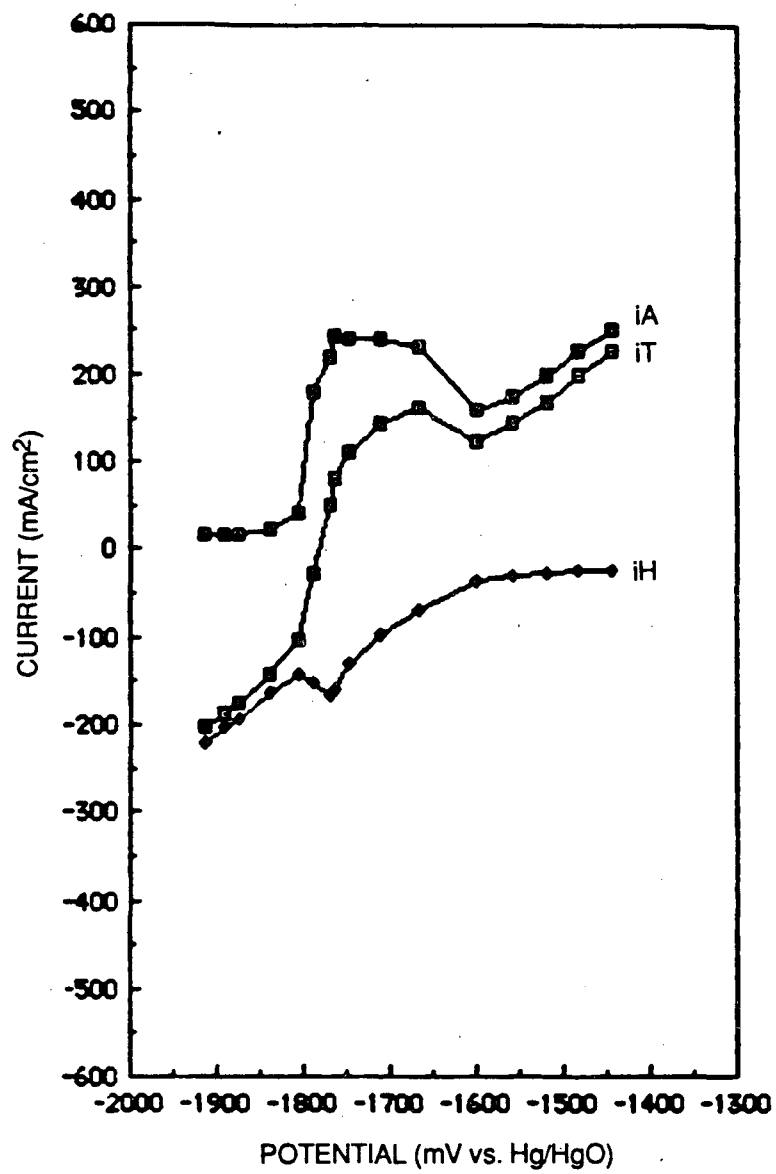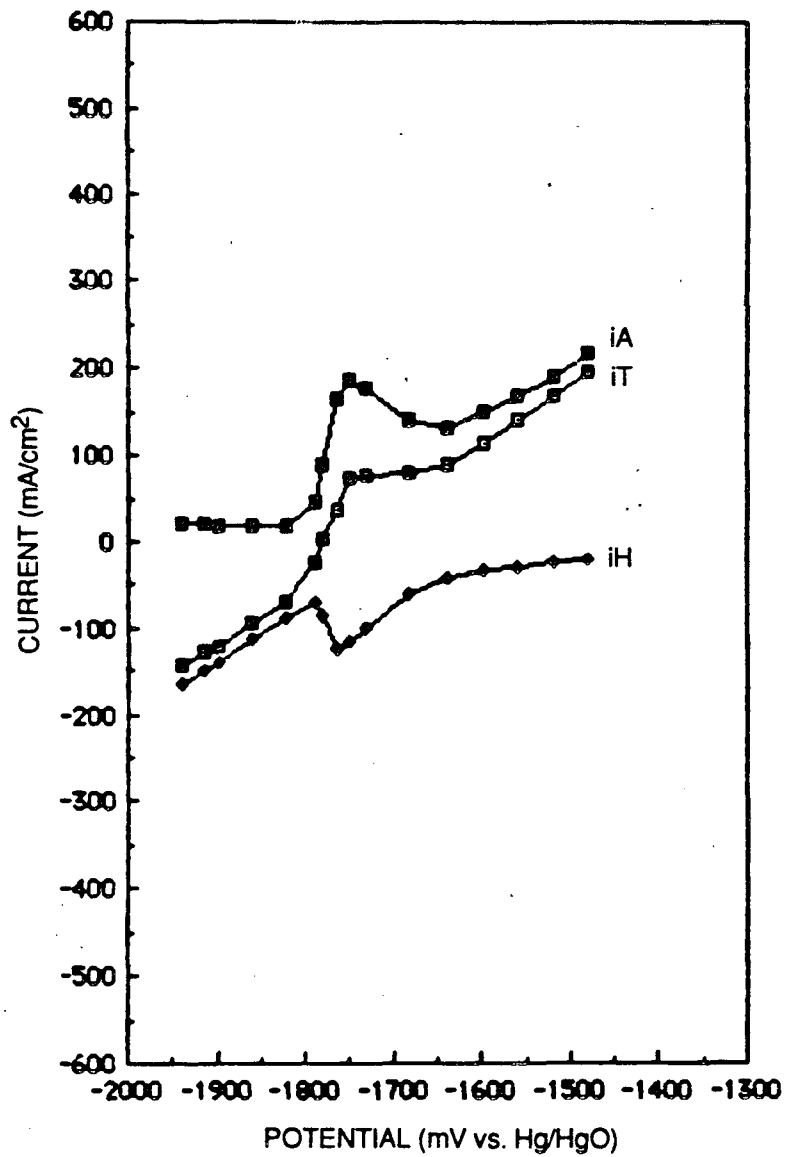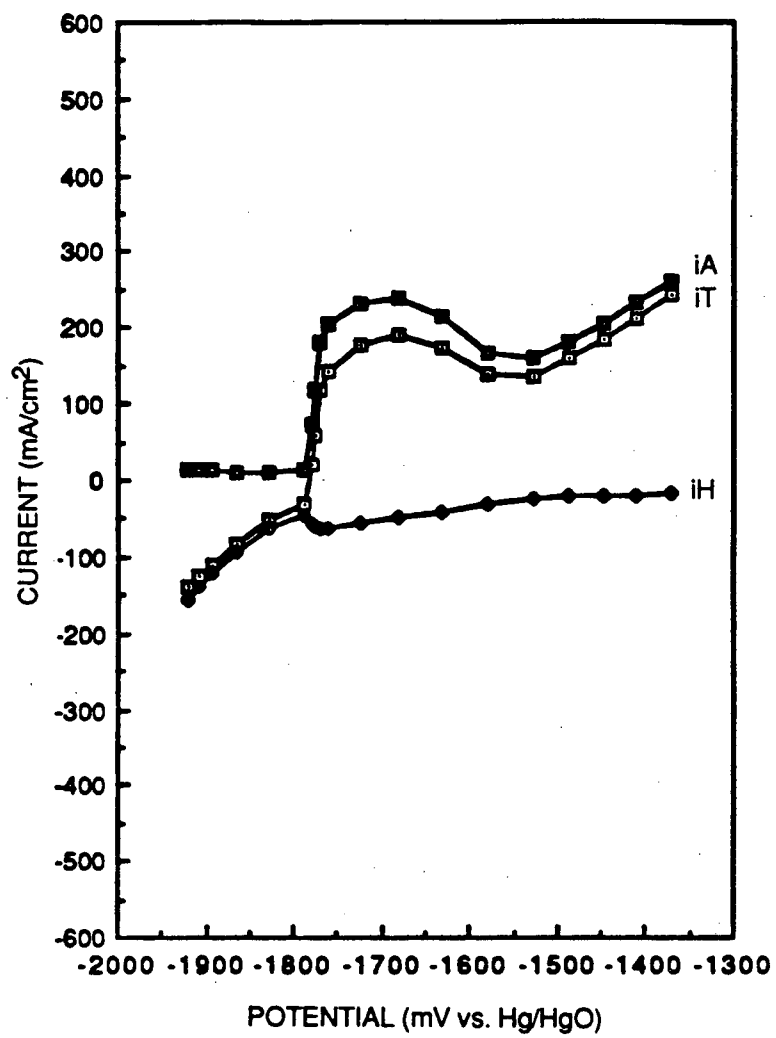
Potential corrected for IR_s drop with $R_s = 0.6\ \Omega$.

53

RA-3357-12

Figure 22. The total current (iT) and delineated anodic (iA) and cathodic (iH) current/voltage curves for Alloy 60533 in 4 M KOH at 50°C.

Potential corrected for IR_s drop with $R_s = 0.6 \, \Omega$.
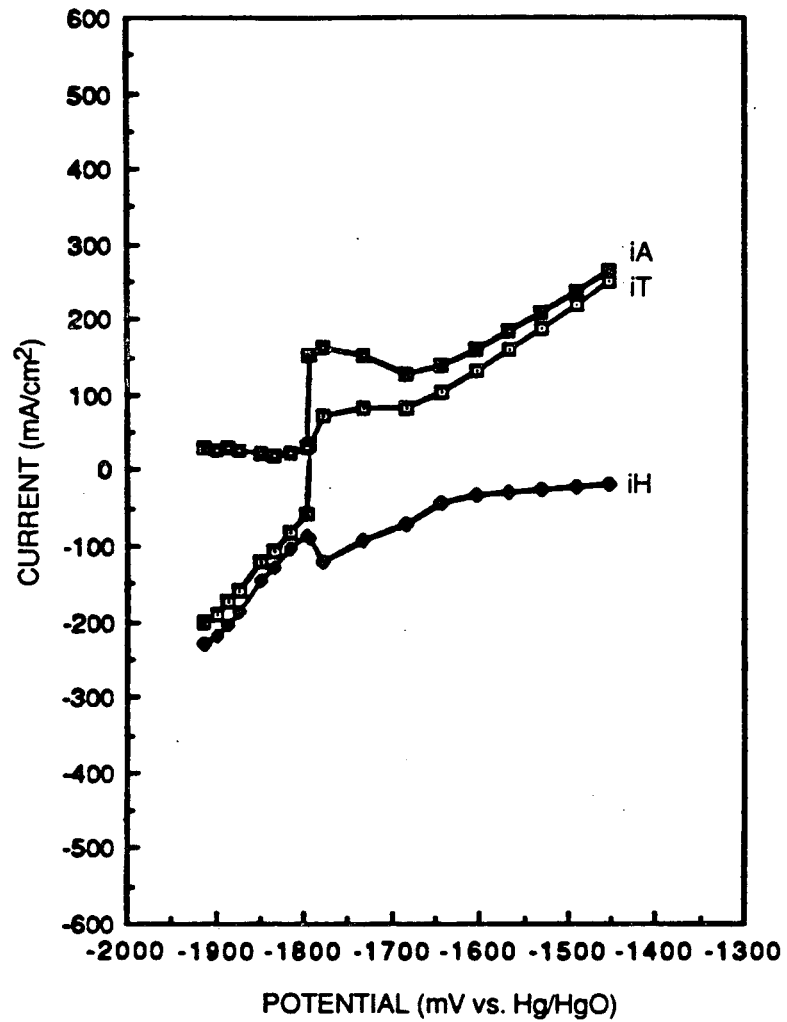
54

RA-3357-13

Figure 23. Steady state polarization curves for Alloy 60535 in
4 M KOH, 50°C, showing the total (iT) current and both
anodic (iA) and cathodic (iH) partial currents.

Potential corrected for IR_s drop with $R_s = 0.6\ \Omega$.

55

RA-3357-14

Figure 24. Steady state polarization curves for Alloy 60537 in
4 M KOH, 50°C, showing the total (iT) current and
both anodic (iA) and cathodic (iH) partial currents.

Potential corrected for IR_s drop with $R_s = 0.6\ \Omega$.

Figure 25. The total current (iT) and delineated anodic (iA) and
cathodic (iH) current/voltage curves for Alloy 60539
in 4 M KOH at 50°C.

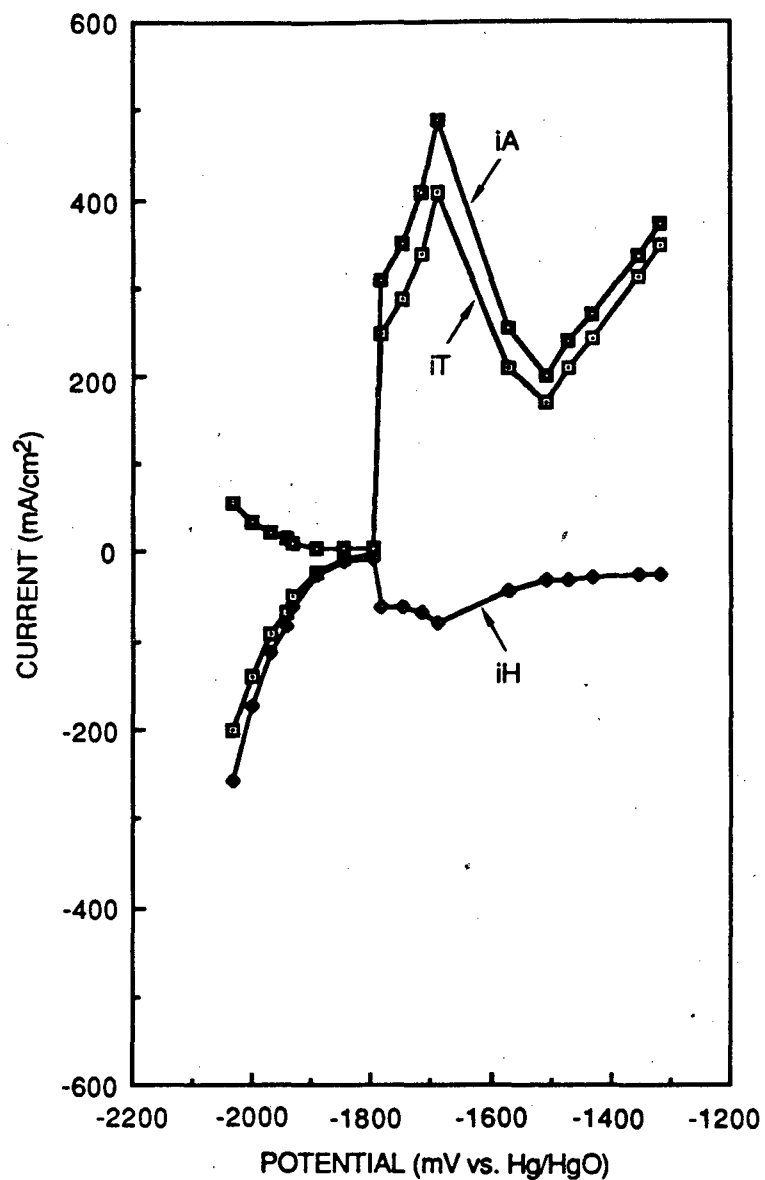Potential corrected for IR_s drop with $R_s = 0.6\ \Omega$.

RA-3357-16

Figure 26. The total current (iT) and delineated anodic (iA) and cathodic (iH) current/voltage curves for Alloy 60540 in 4 M KOH at 50°C.

Potential corrected for IR_s drop with $R_s = 0.6\ \Omega$.

58

JA-m-7572-95

Figure 27. Steady state polarization curves for alloy BDW in 4 M
KOH at 50°C showing the total (iT) current and both
anodic (iA) and cathodic (iH) partial currents.

Potential corrected for IR_s drop with R_s = 1.2 Ω.

more positive potentials due to the formation of $Mg(OH)_2$ on the surface (10). The hydrogen evolution current also exhibits a discontinuity at the activation potential, as previously observed (10,12). The discontinuity is such that, at potentials more negative than E_{crit}, the surface is less catalytic toward hydrogen evolution than that at more positive potentials. This implies that hydrogen evolution on manganese is slower than on aluminum at the critical activation potential; however, considerable care must be taken in attempting to interpret there data in terms of exchange current densities because of the large variance in the Tafel constant (10).

The open circuit corrosion rates of the Group 3 alloys are clearly much lower than those for alloys from Groups 1 and 2. However, the rates are considerably higher than those for the best alloys investigated previously (Table 7), including Alloy BDW. We attribute this discrepancy to thermal processing of Alloy BDW, which presumably was not applied to the other alloys (at least not the same treatment). Finally, the corrosion rates are still too high for these alloys to be considered fully practical as fuels for alkaline Al/air batteries.

D. **Electrochemical Impedance Spectroscopy**

In our previous work (11,12), we conducted extensive experimental electrochemical impedance spectroscopic (EIS) studies of pure aluminum and of the alloys listed in Table 7. These studies also included theoretical analyses of the EIS data, with the objectives of (1) identifying appropriate mechanisms for the corrosion of the alloys in concentrated alkaline media and (2) deriving appropriate kinetic parameters (rate constants, transfer coefficients) that can describe the electrochemical behavior over a wide potential range under steady state conditions and in the frequency domain. This previous work concentrated on interpreting the electrochemistry of pure aluminum in alkaline media in terms of a single mechanism. Over the past year, we expanded this study to include other reaction schemes to incorporate other hydrogen evolution mechanisms and to recognize the possible existence of autocatalytic processes on the surface.

60

Only our theoretical work on analyzing the electrochemistry of pure aluminum in 4 M KOH is reported here. The extensive EIS data that we measured for the various alloys in this medium at 50°C, are not presented at this time because their theoretical interpretation is not sufficiently well—developed. However, the data will be retained in our files so that they may be used later to choose between various theoretical models for the corrosion and electrodissolution of the alloys.

Six mechanisms were proposed to simulate the experimental data for aluminum dissolution and hydrogen evolution in 4 M KOH solution at 25°C. The mechanism are listed in Table 8 and include

    I   Irreversible coupled dissolution/hydrogen ion-atom evolution

   II   Coupled dissolution/H-atom recombination.

 III   Autocatalytic (I)/hydrogen ion-atom evolution

  IV   Autocatalytic (I)/H-atom recombination

   V   Autocatalytic (II)/H-atom recombination

  VI   Autocatalytic (II)/hydrogen ion-atom evolution.

Theoretical impedance spectra for each of these mechanisms were derived using the method of Armstrong, which is described in detail by Macdonald (23). The application of these techniques to the analysis of Mechanism (I) can be found in previous reports (11,12).

Mechanism I was used to simulate the experimentals results obtained with pure aluminum in 4 M KOH at 25°C. The calculated impedance and current/voltage response was found to coincide remarkably well with the experimental measurements (11,12). Specifically, we were able to simulate the current/voltage curves including those for the total current, hydrogen evolution current, and aluminum dissolution current. We could also simulate the impedance (Nyquist) diagrams at each potential, reproducing their shapes and frequency distributions using only one set of parameters for the rate coefficients and Tafel constants for each of the reactions considered (Table 9).

61

Table 8

THEORETICAL MODELS FOR THE CORROSION AND ELECTRODISSOLUTION
OF ALUMINUM ALLOYS IN ALKALINE SOLUTIONS

Mechanism	Reaction Scheme
I Irreversible coupled dissolution/hydrogen ion-atom evolution	$Al(SS)^* + OH^- \xrightarrow{k_1} Al(OH)_{ads} + e^-$ $Al(OH)_{ads} + OH^- \xrightarrow{k_2} Al(OH)_{2,\ ads} + e^-$ $Al(OH)_{2,\ ads} + OH^- \xrightarrow{k_3} Al(OH)_{3,\ ads} + e^-$ $Al(OH)_{3,\ ads} + OH^- \xrightarrow{k_4} Al(OH)_4^-$ $SS + H_2O + e^- \xrightarrow{k_5} H + OH^-$ $H + H_2O + e^- \xrightarrow{k_6} H_2 + OH^- + SS$
II Coupled dissolution/. H-atom recombination	$Al(SS)^* + OH^- \xrightarrow{k_1} Al(OH) + e^-$ $Al(OH) + OH^- \xrightarrow{k_2} Al(OH)_2 + e^-$ $Al(OH)_2 + OH^- \xrightarrow{k_3} Al(OH)_3 + e^-$ $Al(OH)_3 + OH^- \xrightarrow{k_4} Al(OH)_4^- + SS$ $SS + H_2O + e^- \xrightarrow{k_5} H + OH^-$ $H + H \xrightarrow{k_6} H_2 + 2\ SS$
III Autocatalytic (I)/hydrogen Ion-atom evolution	$Al(SS)^* + OH^- \xrightarrow{k_1} Al(OH) + e^-$ $Al(OH) + OH^- \xrightarrow{k_2} Al(OH)_2 + e^-$ $Al(OH)_2 + OH^- \xrightarrow{k_3} Al(OH)_3 + e^-$ $Al(OH)_3 + OH^- \xrightarrow{k_4} Al(OH)_4^- + SS$ $Al(OH)_4^- + Al \xrightarrow{k_c} Al(OH) + Al(OH)_3 + e^-$ $SS + H_2O + e^- \xrightarrow{k_5} H + OH^-$ $H + H_2O + e^- \xrightarrow{k_6} H_2 + OH^- + SS$

62

Table 8 (Concluded)

Mechanism	Reaction Scheme
IV Autocatalytic (I)/H-atom recombination	$Al(SS)^* + OH^- \xrightarrow{k_1} Al(OH) + e^-$ $Al(OH) + OH^- \xrightarrow{k_2} Al(OH)_2 + e^-$ $Al(OH)_2 + OH^- \xrightarrow{k_3} Al(OH)_3 + e^-$ $Al(OH)_3 + OH^- \xrightarrow{k_4} Al(OH)_4^- + SS$ $Al(OH)_4^- + Al \xrightarrow{k_c} Al(OH) + Al(OH)_3 + e^-$ $SS + H_2O + e^- \xrightarrow{k_5} H + OH^-$ $H + H \xrightarrow{k_6} H_2 + 2\ SS$
V Autocatalytic (II)/ H-atom recombination	$Al(SS)^* + OH^- \xrightarrow{k_1} Al(OH) + e^-$ $Al(OH) + OH^- \xrightarrow{k_2} Al(OH)_2 + e^-$ $Al(OH)_2 + OH^- \xrightarrow{k_3} Al(OH)_3 + e^-$ $Al(OH)_3 + OH^- \xrightarrow{k_4} Al(OH)_4^- + SS$ $Al(OH)_4^- + Al \xrightarrow{k_c} Al(OH) + Al(OH)_3 + e^-$ $SS + H_2O + e^- \xrightarrow{k_5} H + OH^-$ $H + H \xrightarrow{k_6} H_2 + 2\ SS$
VI. Autocatalytic (II)/ hydrogen ion-atom evolution	$Al(SS)^* + OH^- \xrightarrow{k_1} Al(OH) + e^-$ $Al(OH) + OH^- \xrightarrow{k_2} Al(OH)_2 + e^-$ $Al(OH)_2 + OH^- \xrightarrow{k_3} Al(OH)_3 + e^-$ $Al(OH)_3 + OH^- \xrightarrow{k_4} Al(OH)_4^- + SS$ $Al(OH)_4^- + Al \xrightarrow{k_c} Al(OH) + Al(OH)_3 + e^-$ $SS + H_2O + e^- \xrightarrow{k_5} H + OH^-$ $H + H_2O + e^- \xrightarrow{k_6} H_2 + OH^- + SS$

*SS represents a base surface site, i.e., Al(SS).

Table 9

PARAMETERS FOR THEORETICAL MODEL FOR ALUMINUM
DISSOLUTION MECHANISM I IN 4 M KOH AT 25°C

Parameter	Value	Units	
k_1°	3.0 E - 2	m^3/s-mol	
k_2°	3.0 E - 4	m^3/s-mol	
k_3°	2.5 E - 4	m^3/s-mol	
k_4°	2.0 E - 4	m^3/s-mol	
k_5°	2.5 E - 4 · $[H_2O]$	m^3/s-mol · mol/m^3	
k_6°	1.0 E - 6 · $[H_2O]$	m^3/s-mol · mol/m^3	
k_c°*	1.0 E - 2	m^3/s-mol	
b_1	3.0	$volt^{-1}$	
b_2	4.0	$volt^{-1}$	
b_3	3.0	$volt^{-1}$	
b_5	4.5	$volt^{-1}$	
b_6	6.7	$volt^{-1}$	
b_c	3.0	$volt^{-1}$	
Γ_T (-1.35)[+]	6.06 E - 2	mol/m^2	⎫
Γ_T (-1.38)	6.06 E - 2	mol/m^2	⎪
Γ_T (-1.46)	4.62 E - 2	mol/m^2	⎬ Anodic zone
Γ_T (-1.50)	3.87 E - 2	mol/m^2	⎪
Γ_T (-1.60)	2.37 E - 2	mol/m^2	⎪
Γ_T (-1.64)	1.87 E - 2	mol/m^2	⎭
Γ_T (-1.68)	1.15 E - 2	mol/m^2	⎫
Γ_T (-1.70)	1.05 E - 2	mol/m^2	⎬ Transition zone
Γ_T (-1.74)	0.95 E - 2	mol/m^2	⎭
Γ_T (-1.88)	0.37 E - 2	mol/m^2	⎫
Γ_T (-1.92)	0.87 E - 2	mol/m^2	⎬ Cathodic zone
Γ_T (-1.95)	1.50 E - 2	mol/m^2	⎭
C	0.20	F/m^2	
E_{Al}°	-2.30	volt Vs Hg/HgO	
E_H°	-0.82	volt vs Hg/HgO	
[OH]	4.0 E + 3	mol/m^3	

*k_c° and b_c refer to the catalytic reaction included in Mechanisms III-
VI Table 8.

[+]Γ_T (-1.35) refers to the total concentration of reaction sites on the
surface at -1.35 V (vs Hg/HgO).

The results are shown in Figure 28 through 38. Figure 28 represents the calculated and experimental steady-state current/potential curves. Figures 29 through 38 compare the calculated and experimental Nyquist diagrams at various potentials corresponding to different points on the current/potential curve (Figure 28). These result were extensively discussed in our previous report (12), so only the comparison between theory and experiment will be/presented here. To successfully simulate the impedance data, it was necessary to assume that the total number of active sites on the surface varies with potential, as indicated in Table 9, and that the transfer coefficients are very small. The first assumption was rationalized by noting that the surface is covered with a corrosion product film, whose coverage is itself potential-dependent. This model predicts that Γ_T vs potential should parallel the current voltage curve, which is in fact observed (Table 9, Figure 28).

If we assume a potential-independent value for Γ_T, we can generate the right shapes for the Nyquist diagrams; however, the corresponding maximum and minimum impedances values, as well as the partial currents for hydrogen evolution and aluminum dissolution could not be matched with the experimental results.

We also note that the calculated impedances at intermediate frequencies (i.e., at the loop, Figure 36) apparently do not become inductive, although such behavior is clearly indicated by the experimental data. An inductive response suggests that the impedance (at that frequency) is dominated by relaxations involving adsorbed species, particularly those involved in autocatalytic processes. Autocatalysis is not included in Mechanisms I and II, but it is incorporated in various ways in Mechanisms III through VI (Table 8). Accordingly, the data plotted in Figures 29 through 38, together with the theoretical analyses of Mechanisms I through VI, possibly afford a means of detecting and assessing the importance of autocatalysis in the dissolution of aluminum in alkaline media.

To evaluate the sensitivity of the impedance function calculated from Mechanism I to the values selected for various kinetic parameters (rate
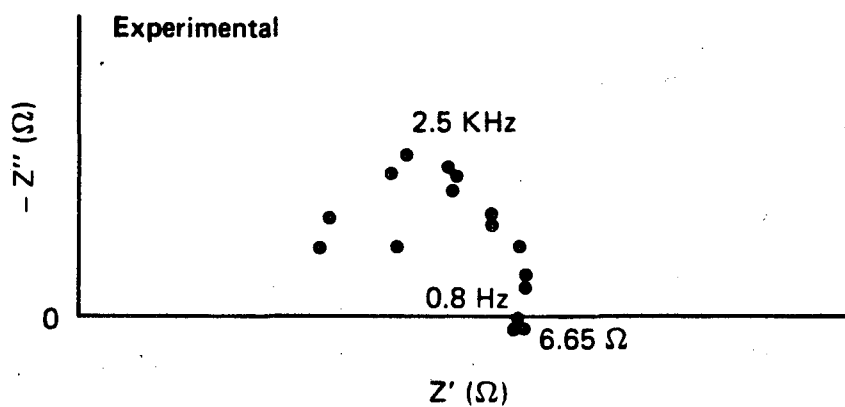
65
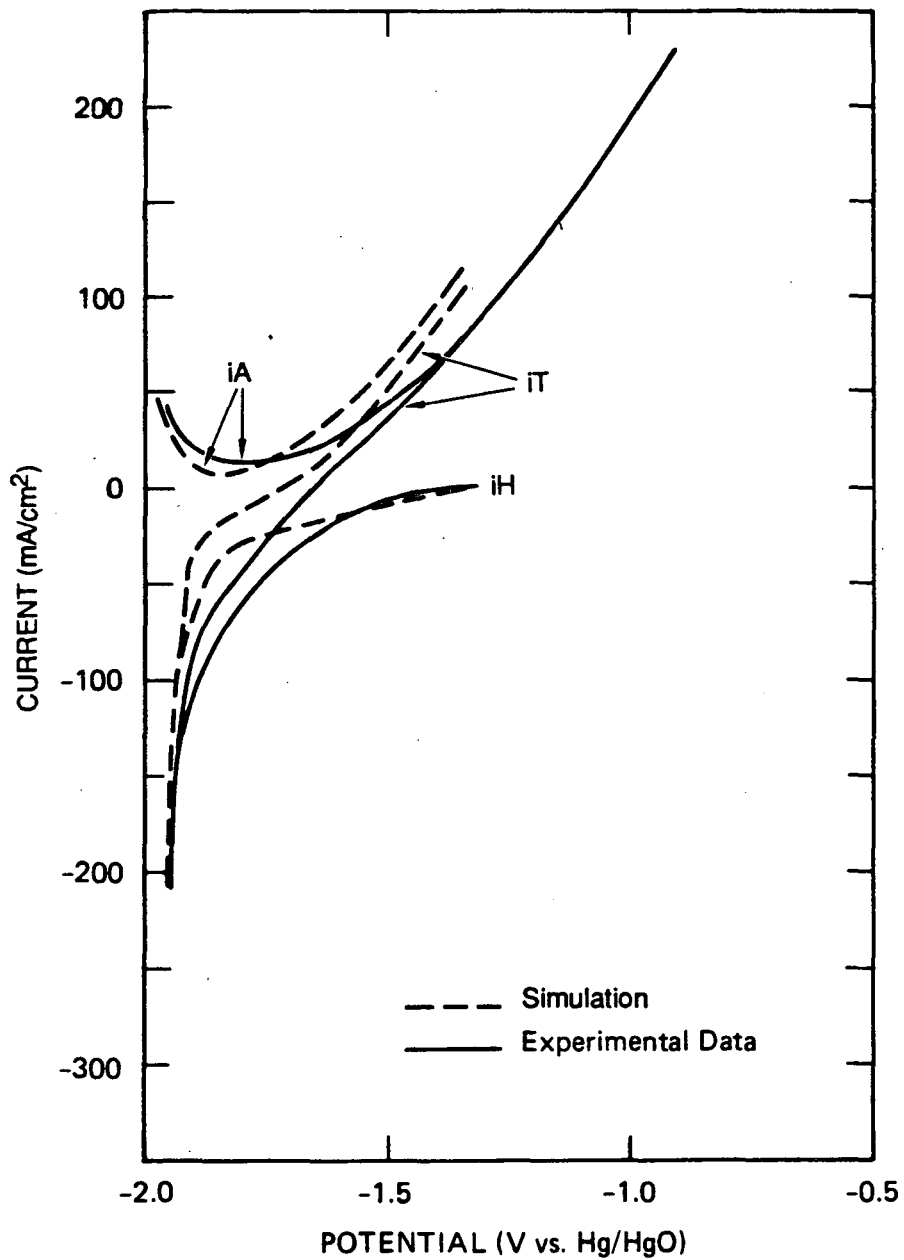
Figure 28. Steady state polarization curves for pure aluminum in 4 M KOH at 25°C showing the experimental and calculated total currents (iT) and both anodic (iA) and cathodic (iH) partial currents.
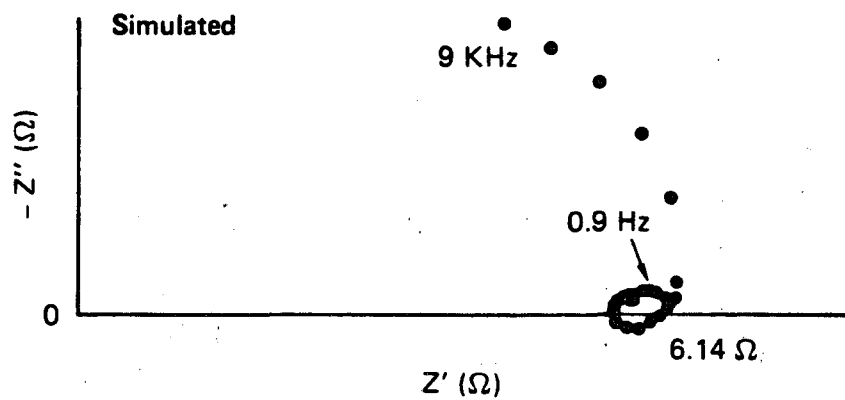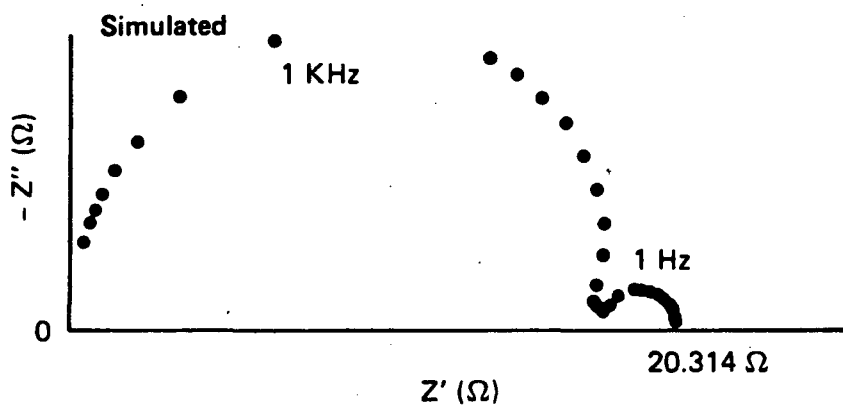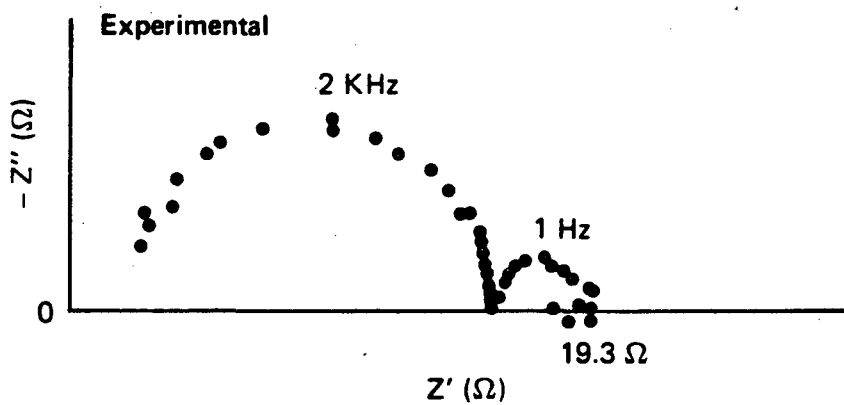
JA-7572-39A

Figure 29. Simulated and experimental Nyquist diagrams for pure aluminum in 4 M KOH at 25°C and at an applied potential of -1.96 V vs Hg/HgO.
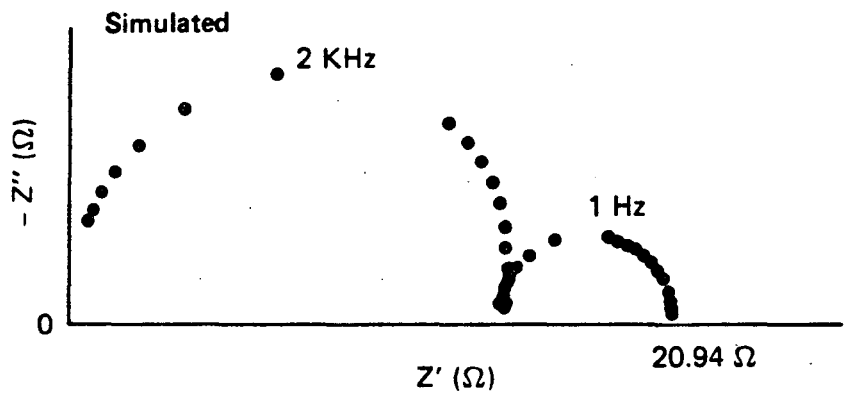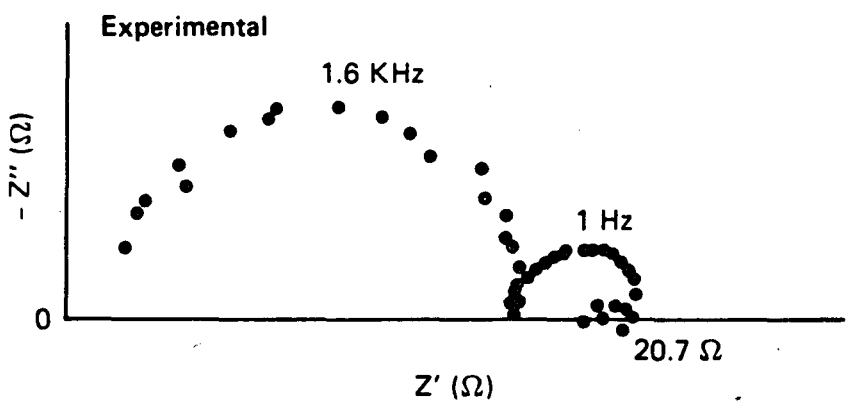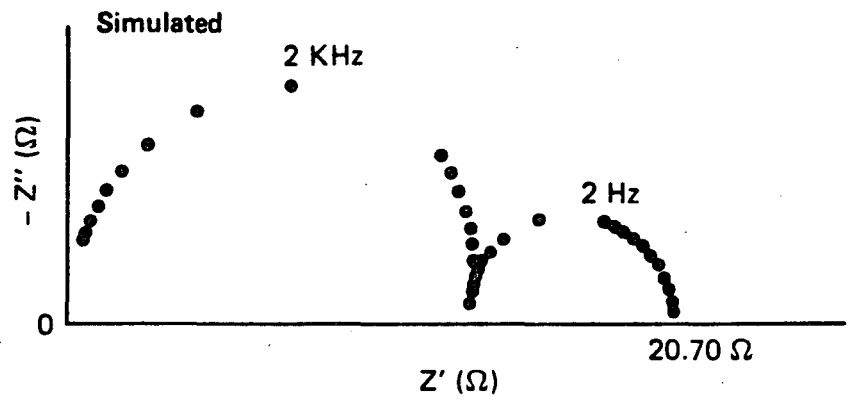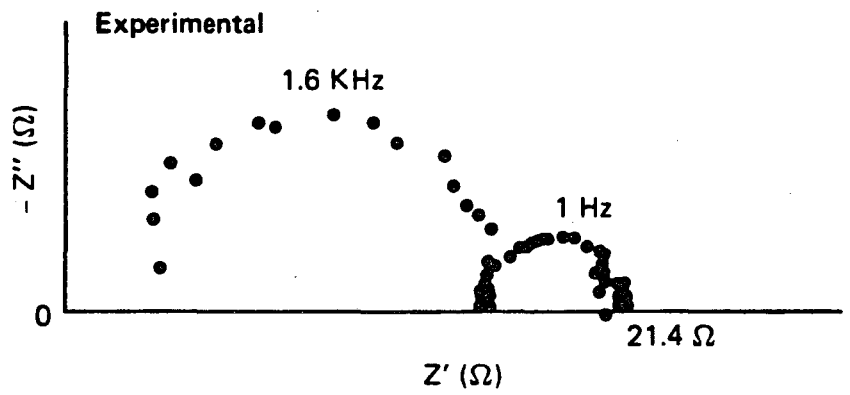
67

(a) E = -1.88 V vs Hg/HgO

(b) E = -1.88 V vs Hg/HgO

JA-m-7572-29A

Figure 30. Simulated and experimental Nyquist diagrams for pure aluminum in 4 M KOH at 25°C and at an applied potential of -1.88 V vs Hg/HgO.
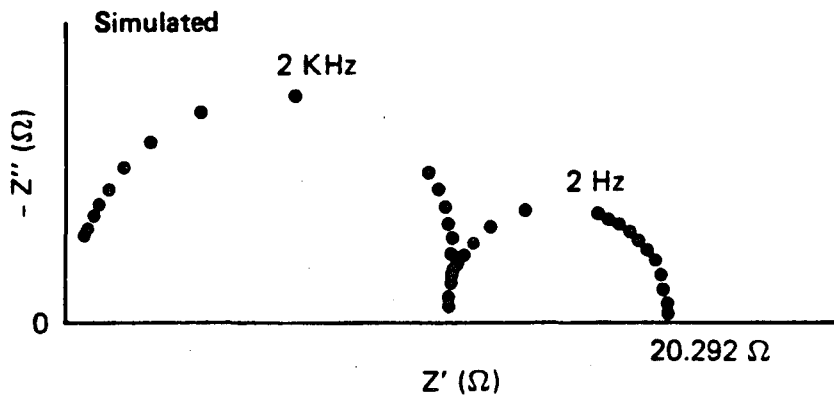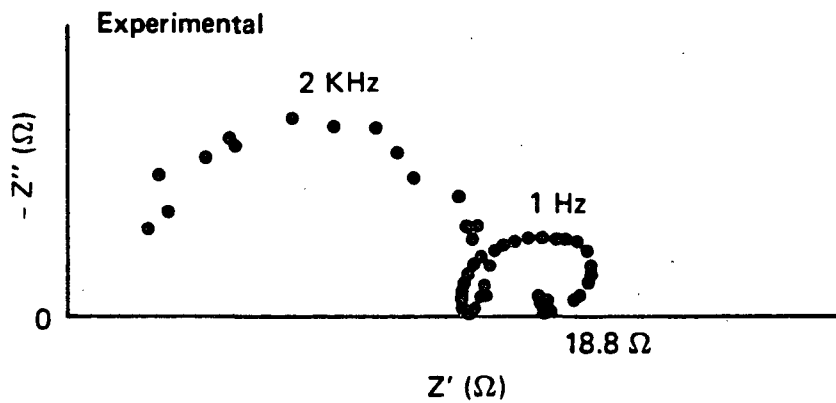
68

Figure 31. Simulated and experimental Nyquist diagrams for pure aluminum in 4 M KOH at 25°C and at an applied potential of -1.74 V vs Hg/HgO.

Figure 32. Simulated and experimental Nyquist diagrams for pure aluminum in 4 M KOH at 25°C and at an applied potential of -1.70 V vs Hg/HgO.

Simulated

- Z'' (Ω)

2 KHz

2 Hz

0

20.292 Ω

Z' (Ω)

(a) E = -1.68 V vs Hg/HgO

Experimental

- Z'' (Ω)

2 KHz

1 Hz

0

18.8 Ω

Z' (Ω)

(b) E = -1.68 V vs Hg/HgO

JA-m-7572-32A

Figure 33. Simulated and experimental Nyquist diagrams for pure
aluminum in 4 M KOH at 25°C and at an applied potential of
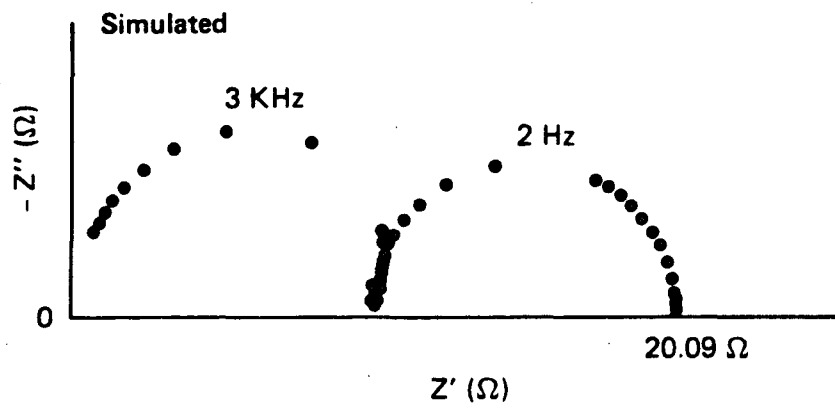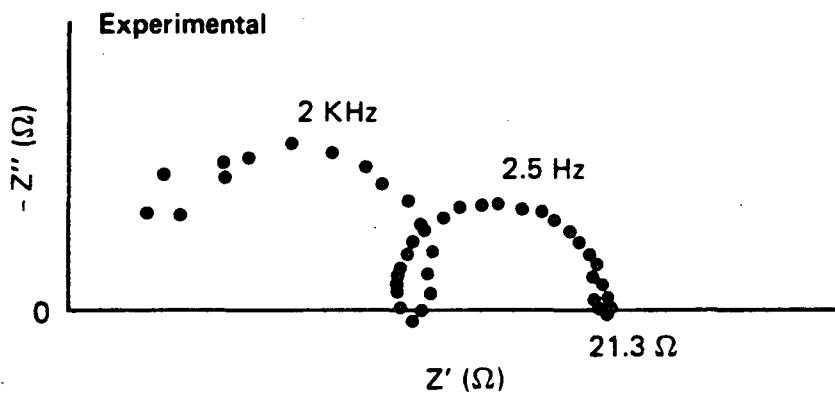-1.68 V vs Hg/HgO.

71

Simulated

3 KHz

2 Hz

$-Z''$ (Ω)

0

20.09 Ω

Z' (Ω)

(a) E = -1.6 V vs Hg/HgO

Experimental

2 KHz

2.5 Hz

$-Z''$ (Ω)

0

21.3 Ω

Z' (Ω)

(b) E = -1.6 V vs Hg/HgO

JA-m-7572-34A

Figure 34. Simulated and experimental Nyquist diagrams for pure
aluminum in 4 M KOH at 25°C and at an applied potential of
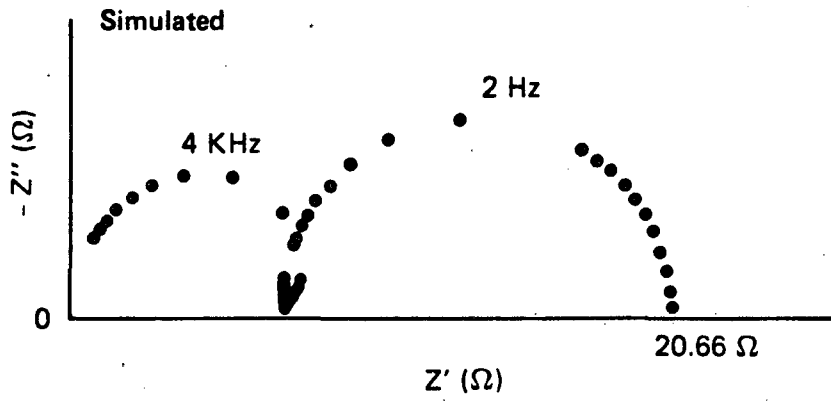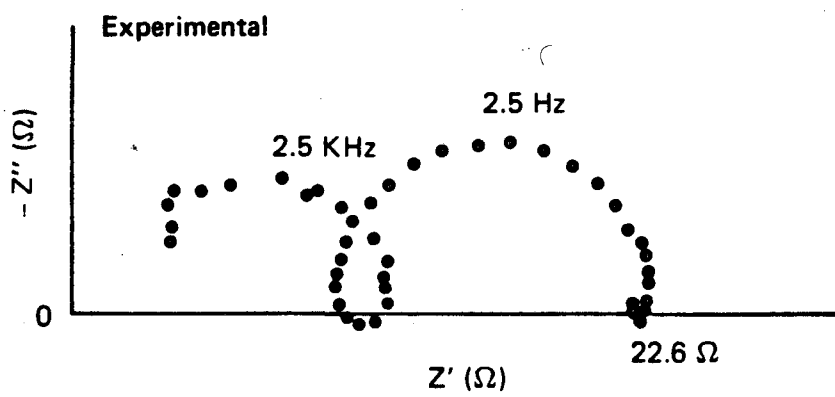-1.60 V vs Hg/HgO.

(a) E = -1.5 V vs Hg/HgO

(b) E = -1.5 V vs Hg/HgO

JA-m-7572-35A

Figure 35.   Simulated and experimental Nyquist diagrams for pure
aluminum in 4 M KOH at 25°C and at an applied potential of
-1.50 V vs Hg/HgO.

73

Simulated

2 Hz

4 KHz

0

20.59 Ω

Z' (Ω)

$-Z''$ (Ω)

(a) E = -1.46 V vs Hg/HgO

Experimental

2 Hz

4 KHz

0

22.3 Ω

Z' (Ω)

$-Z''$ (Ω)

(b) E = -1.46 V vs Hg/HgO

JA-m-7572-36A

Figure 36. Simulated and experimental Nyquist diagrams for pure
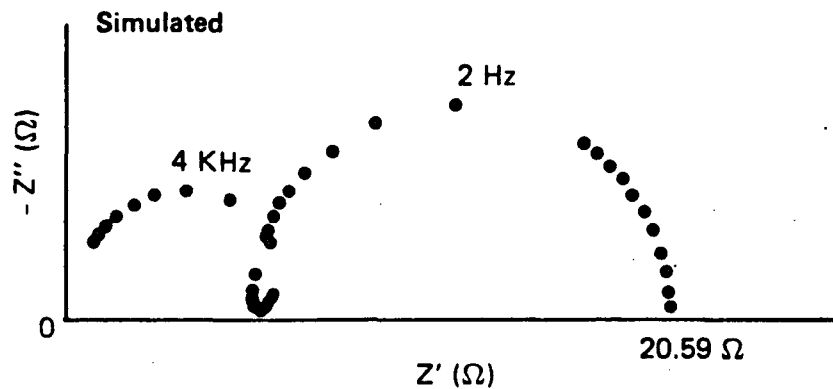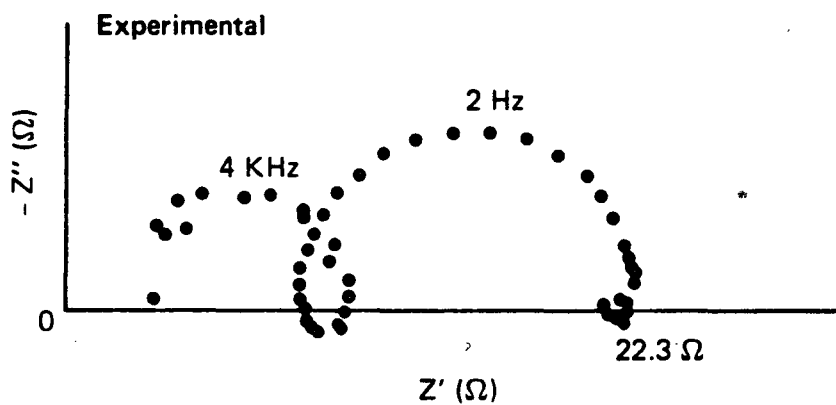aluminum in 4 M KOH at 25°C and at an applied potential of
-1.46 V vs Hg/HgO.

Figure 37. Simulated and experimental Nyquist diagrams for pure aluminum in 4 M KOH at 25°C and at an applied potential of -1.38 V vs Hg/HgO.

Figure 38. Simulated and experimental Nyquist diagrams for pure aluminum in 4 M KOH at 25°C and at an applied potential of -1.35 V vs Hg/HgO.

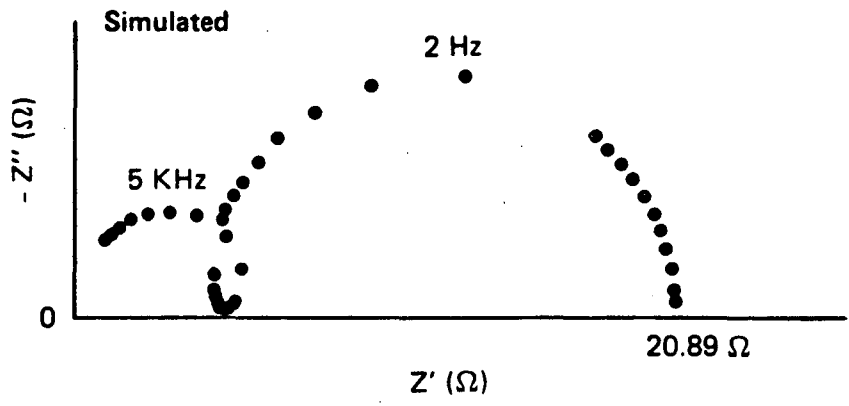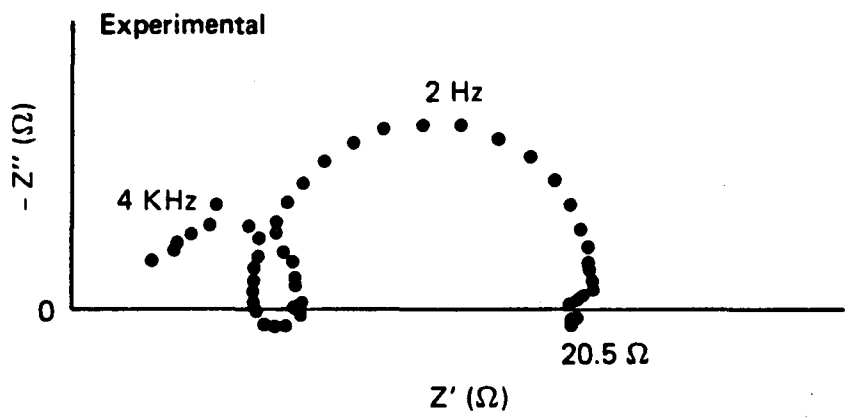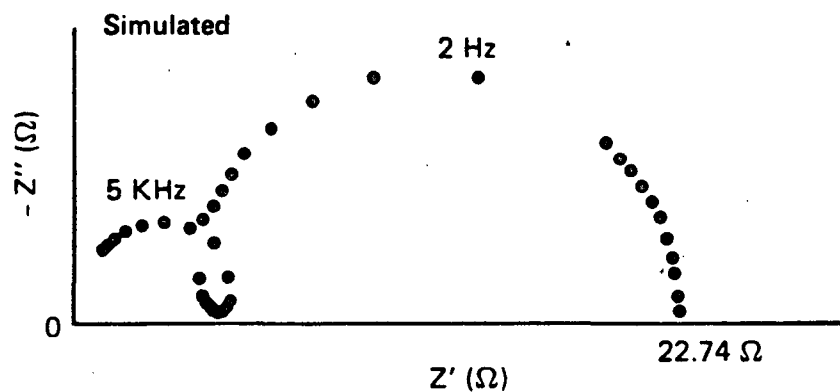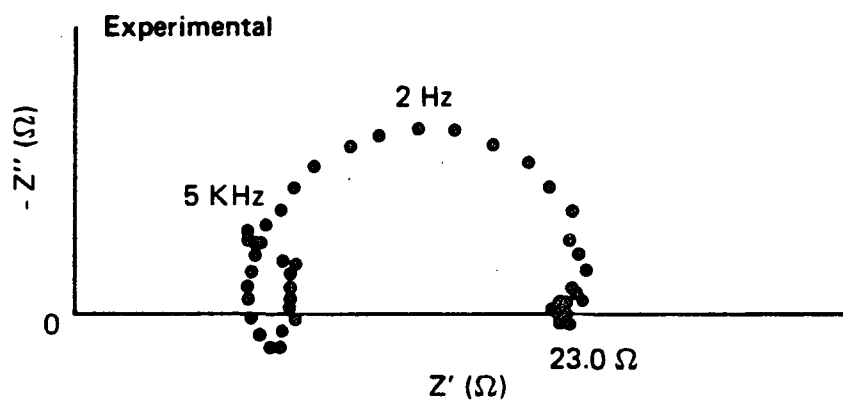constants, k_i, and Tafel constants, b_i) and to the assumption that the
surface is partially covered by a corrosion product film, we calculate
impedance spectra in which the k_i° and b_i parameters are increased or
decreased by a factor of 10 or by one unit, respectively. We also
compute impedance spectra assuming that no corrosion product exists on
the surface. Characteristic parameters calculated on the basis of the
above are summarized in Tables 10 and 11. The base case plotted in
Figures 28 through 38 corresponds to the second entries titled "Film on
Surface." Changing the rate constants by a factor of 10 or varying the
Tafel constants by ± 1 (see Table 9) causes large changes in the
impedance parameters and/or the steady state partial anodic (aluminum
dissolution), cathodic (hydrogen evolution), and total currents.
However, the general shapes of the impedance loci in the complex plane
are not highly sensitive to these changes, with the exception of the
last entry in Table 11. Clearly, it is the frequency distribution of
the impedance parameters that is important in choosing between various
mechanisms; hence it is probably more efficient to conduct the
comparison between theory and experiment in both the Nyquist and Bode
($\log |Z|$, ϕ vs $\log \omega$) planes.

Possibly the best way of exploring various mechanisms is to compare
both the calculated frequency and potential dependence of the impedance
with those observed experimentally. Using the kinetic parameters
contained in Table 9, we display in Table 12 Nyquist diagrams for the
six mechanisms of interest and the corresponding experimental data for
five potentials spanning the anodic and cathodic potential regions.
More detailed comparisons between the six mechanisms and the
experimental data at two potentials are shown in Table 13 and 14.
Comparison of the calculated and experimental impedance and steady-state
data reveals that Mechanism I provides the best description of the
electrochemistry of aluminum in 4 M KOH at 25°C by reproducing the
impedance function quite accurately as a function of frequency and
potential (Figures 29 through 38) and by reasonably simulating the
steady-state current/voltage curves.

A principal reason for exploring other mechanisms was to explain
the inductive nature of the loop at intermediate frequencies (e.g.,

Table 10

SENSITIVITY STUDY FOR CALCULATED IMPEDANCE VALUES AND PARTIAL AND TOTAL CURRENT DENSITIES FOR MECHANISM I. POTENTIAL = -1.64 mV vs SHE. (ALUMINUM IN 4M KOH, 25°C)

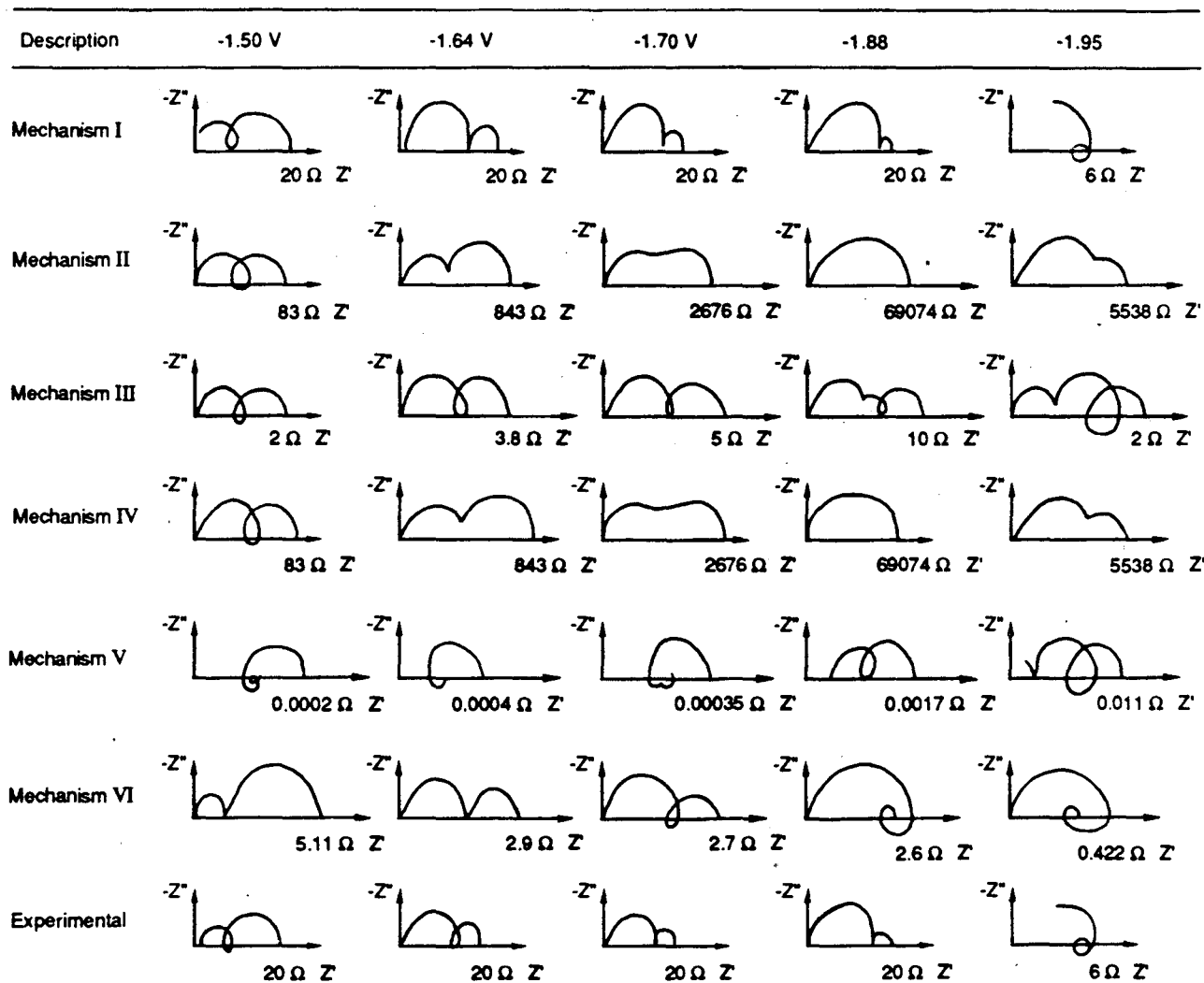| Description	$\omega(-Z''_{MAX})$ (Hz)	Z'_{MAX} (Ω)	$-Z''_{MAX}$ (Ω)	H_2 Current (mA/cm^2)	Al Current (mA/cm^2)	Total current (mA/cm^2)
Experimental value	2000	20.80	6.40	-23	+33	+10
Film on surface[a]	2000	20.11	6.68	-22	+34	+12
No film on surface[a]	2500	15.21	5.22	-29	+46	+17
Film on surface and rate constants * 10[a]	25000	2.02	0.67	-220	+347	+127
Film on surface and rate constants/10[a]	1200	202	67	-2.2	+3.4	+1.2
Film on surface and Tafel constants +1[a]	18000	14.7	4.9	-26	+34	+8
Film on surface and Tafel constants -1[a]	12000	29.6	9.6	-18	+34	+15

[a]Same shape.

78

Table 11

SENSITIVITY STUDY FOR CALCULATED IMPEDANCE VALUES, AND PARTIAL AND
TOTAL CURRENT DENSITIES FOR MECHANISM I. POTENTIAL = -1.96 mV
vs SHE (ALUMINUM IN 4 M KOH, 25°C)

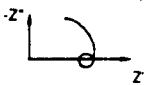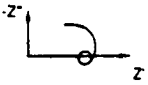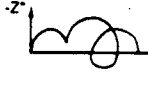| Description	$\omega(-Z''_{MAX})$ (Hz)	Z'_{MAX} (Ω)	$-Z''_{MAX}$ (Ω)	H_2 Current (mA/cm^2)	Al Current (mA/cm^2)	Total current (mA/cm^2)
Experimental value	2500	6.65	3.35	-160	+40	-120
Film on surface[a]	9000	6.14	3.12	-177	+27	-150
No film on surface[a]	125000	1.9	0.92	-296	+45	-251
Film on surface and rate constants * 10[a]	565000	0.312	0.16	-1778	+272	-1506
Film on surface and rate constants/10[a]	5600	31.25	16.17	-17.78	+2.72	-15
Film on surface and Tafel constants +1[a]	125000	1.26	0.65	-391	+27	-363
Film on surface and Tafel constants -1[a]	2500	7.9	3.99	-80	+27	-53

[a]Same shape.

79
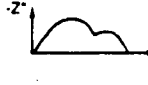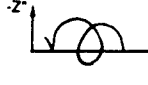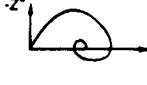
Table 12

NYQUIST DIAGRAMS CALCULATED WITH THE SET OF PARAMETERS SHOWN IN TABLE 9 COMPARED WITH EXPERIMENTAL VALUES FOR ALUMINUM 4 M KOH AT 25°C

POTENTIAL (vs. SHE)

Description	-1.50 V	-1.64 V	-1.70 V	-1.88	-1.95
Mechanism I	20 Ω Z'	20 Ω Z'	20 Ω Z'	20 Ω Z'	6 Ω Z'
Mechanism II	83 Ω Z'	843 Ω Z'	2676 Ω Z'	69074 Ω Z'	5538 Ω Z'
Mechanism III	2 Ω Z'	3.8 Ω Z'	5 Ω Z'	10 Ω Z'	2 Ω Z'
Mechanism IV	83 Ω Z'	843 Ω Z'	2676 Ω Z'	69074 Ω Z'	5538 Ω Z'
Mechanism V	0.0002 Ω Z'	0.0004 Ω Z'	0.00035 Ω Z'	0.0017 Ω Z'	0.011 Ω Z'
Mechanism VI	5.11 Ω Z'	2.9 Ω Z'	2.7 Ω Z'	2.6 Ω Z'	0.422 Ω Z'
Experimental	20 Ω Z'	20 Ω Z'	20 Ω Z'	20 Ω Z'	6 Ω Z'

RA-m-3357-17

80
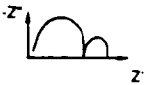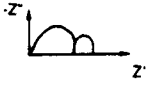
Table 13
EXPERIMENTAL AND THEORETICAL NYQUIST DIAGRAMS AND PARTIAL AND TOTAL CURRENT DENSITIES FOR ALUMINUM in 4 M KOH AT 25°C, AND AT A POTENTIAL OF -1.96 V vs SHE

	$\omega(Z_{R, MAX})$ (Hz)	$Z_{R, MAX}$ (Ω)	$-Z_{i, MAX}$ (Ω)	H_2 Current (mA/cm^2)	Al Current (mA/cm^2)	Total Current (mA/cm^2)	Shape
Experimental	2500	6.65	3.35	-160	+40	-120	
Mechanism I	9000	6.14	3.12	-177	+27	-150	
Mechanism II	12	5538.6	1819.8	-0.24	+0.109	-0.13	
Mechanism III	1250	2.13	0.52	-625.6	+285.7	-339.8	
Mechanism IV	50	5538.6	1819.8	-0.24	+0.109	-0.13	
Mechanism V	1200	0.011	0.0027	-114855	+52467	-62388	
Mechanism VI	376000	0.44	0.22	-179	+197	18.51	

RA-m-3357-18

81

Table 14

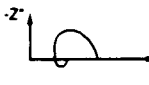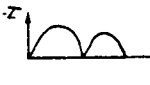EXPERIMENTAL AND THEORETICAL NYQUIST DIAGRAMS AND PARTIAL AND TOTAL
CURRENT DENSITIES FOR ALUMINUM IN 4 M KOH AT 25°C, AND AT A POTENTIAL
OF -1.64 V vs SHE

	$\omega (Z_{R, MAX})$ (Hz)	$Z_{R, MAX}$ (Ω)	$-Z_i, MAX$ (Ω)	H_2 Current (mA/cm^2)	Al Current (mA/cm^2)	Total Current (mA/cm^2)	Shape
Experimental	2000	20.80	6.40	-23	+33	+10	
Mechanism I	2000	20.11	6.68	-22	+34	+12	
Mechanism II	6.2	843.8	223.8	-0.37	+1.72	+1.37	
Mechanism III	628	3.68	0.975	-85	+399	+314	
Mechanism IV	6.2	843.8	223.8	-0.37	+1.74	+1.32	
Mechanism V	6.2	0.0004	0.00011	-890294	+4.15 x 10^6	+3.26 x 10^6	
Mechanism VI	628	2.93	0.768	-171	+399	+228	

RA-m-3357-19

82

Figures 36 through 38). Clearly, Mechanisms III, IV, V, and VI are capable of explaining the inductive behavior, which is attributed to the presence of autocatalytic reactions on the surface. However, none of these mechanisms appears to be capable of reproducing the other characteristics of the impedance function, so the origin of the inductive behavior remains unclear.

E. Effect of Hydroxide Concentration

One objective of our current work was to explore the effect of hydroxide concentration on the electrochemistry of aluminum in alkaline solutions. An extensive study of this type would yield valuable mechanistic data including the reaction order with respect to OH^-. However, out work was planned to be only a preliminary study to explore the gross changes in the electrochemical behavior over a limited range of hydroxide concentration. These preliminary studies could not be completed because the collection efficiency of the porous anode for hydrogen oxidation downstream from the aluminum specimen was found to be irreproduceible at the lower KOH concentration (1M) used. We believe that this limitation is not inherent in the technique, but rather that it was caused by a change in the catalytic properties of the platinum-activated porous nickel hydrogen collector electrode.

VI SUMMARY AND CONCLUSIONS

We have explored the electrochemistry of various Al-Li-In, Al-Li-In-Bi, and Al-Mg-Mn-In alloys in 4 M KOH at 50°C by delineating the partial anodic and cathodic processes as a function of potential spanning the hydrogen evolution and alloy dissolution ranges. The principal findings are as follows:

(1)   The Al-Li-In (Group I) alloys exhibit very high corrosion rates under open circuit conditions, and are therefore not suitable as fuels for aluminum/air batteries. The alloys do not exhibit the desired activation phenomenon because they lack an alloying element that oxidizes to form a soluble product within the potential range of interest.

(2)   The Al-Li-In-Bi (Group II) alloys also exhibit high corrosion rates under open circuit conditions and hence are judged to be unsuitable as fuels for alkaline Al/air batteries. Bismuth does not give rise to an activation phenomenon and does not appear to yield any particularly advantageous characteristics over the simpler Al-Li-In system.

(3)   Group III alloys (Al-Mg-Mn-In) exhibit activation at potentials within the range -1.75 to -1.85 V (vs Hg/HgO, 4 M KOH) at 50°C, associated with the oxidation of manganese from the surface. However, all alloys in this group passivate at more positive potentials, followed by a region where the current varies nearly linearly with voltage. These same characteristics are exhibited by Alloy BDW (Al-1Mg-0.1In-0.2Mn), which has been proposed by ALCAN as a fuel for alkaline aluminum/air batteries and which we investigated previously. None of the alloys studied in the present program appears to offer any advantages over Alloy BDW as a fuel for alkaline aluminum/air batteries.

We have also continued to analyze various mechanisms to account for the extensive impedance data for pure aluminum in 4 M KOH at 25°C that we reported previously. Six mechanisms were explored, including some that involve autocatalytic reactions in the aluminum electrodissolution process. None of these mechanisms appears to be capable of accounting for the measured impedance better than the simple irreversible coupled dissolution/hydrogen ion-atom evolution mechanism reported earlier. Although these latter mechanisms can account for the inductive behavior

at intermediate frequencies, they do not seem to explain other features of the impedance as a function of frequency and applied potential or the steady-state partial anodic and cathodic current/voltage curves.

REFERENCES

1. J. F. Cooper, R. V. Homsy, and J. H. Landrum, "The Aluminum-Air Battery for Electric Vehicle Propulsion," Proceedings of the 15th Intersociety Energy Conversion Engineering Conference (1980).

2. J. D. Salisbury, E. Rehrir, M. K. Kong, and D. J. Whisler, "A Comparative Analysis of Aluminum-Air Battery Propulsion Systems for Passenger Vehicles," UCRL 52933, University of California, Lawrence Livermore Laboratory Report (1980).

3. A. J. Salkind, "Aluminum-air Battery System. Assessment of Technical and Market Viability for Electric Vehicle Applications," Final Report to DOE, Contract No. 5-23558 (1980).

4. C. J. McMinn and J. A. Branscomb, "Production of Anodes for Aluminum-Air Power Cells Directly from Hall Cell Metal," Report to DOE, Subcontract No. 6124909 (1981).

5. A. R. Despic, D. M. Drazic, M. M. Purenovic, and N. Cikovic, J. Appl. Electrochem., $\underline{6}$, 527 (1976).

6. Y. Hori, J. Takao, and H. Shomon, Electrochim. Acta, $\underline{30}$, 1121 (1985).

7. K. F. Blurton and A. F. Sammells, J. Powers Sources, $\underline{4}$, 263 (1979).

8. D. D. Macdonald, K. H. Lee, A. Moccari, and D. Harrington, "Evaluation of Alloy Anodes for Aluminum-Air Batteries. I Corrosion Studies," Corrosion, submitted for publication (1987).

9. S. Real, M. Urquidi-Macdonald, and D. D. Macdonald, "Evaluation of Alloy Anodes for Aluminum-Air Batteries. II Delineation of Anodic and Cathodic Partial Reactions," J. Electrochem. Soc., submitted for publication (1987).

10. D. D. Macdonald, S. Real, and M. Urquidi-Macdonald, "Evaluation of Alloy Anodes for Aluminum-Air Batteries. III Mechanisms of Activation, Passivation, and Hydrogen Evolution," J. Electrochem. Soc., submitted for publication (1987).

11. D. D. Macdonald, S. Real, S. I. Smedley, and M. Urquidi-Macdonald, "Evaluation of Alloy Anodes for Aluminum-Air Batteries. IV Electrochemical Impedance Analysis of Pure Aluminum in 4 M KOH at 25°C." J. Electrochem. Soc., submitted for publication (1987).

12. D. D. Macdonald, S. Real, and M. Urquidi-Macdonald, "Development and Evaluation of Anode Alloys for Aluminum/Air Batteries," Final Report to Eltech Systems/DOE, Subcontract 100484-MLM, 1987.

13. D. D. Macdonald, K-H. Lee, A. Moccari, D. Harrington, and M. Urquidi, "The Metallurgy and Electrochemistry of the Aluminum

Anode," report to Eltech Systems Corp. from Ohio State University, FCC 5162, May 10, 1984.

14. M.C.H. McKubre and D. D. Macdonald, J. Electrochem. Soc., $\underline{128}$, 524 (1981).

15. R. Greef and C.F.W. Norman, J. Electrochem. Soc., $\underline{132}$, 2362 (1985).

16. O. R. Brown and J. S. Whitley, Electrochim. Acta, $\underline{32}$, 545 (1987).

17. K. E. Heusler and W. Allgaier, Werkst. Korros., $\underline{22}$, 297 (1971).

18. D. D. Macdonald, B. Pound, R. P. Singh, and B. Sundararaj, "Thermodynamic Framework for Estimating the Efficiencies of Alkaline Batteries," Report FCC 2822-9 to LBL, Univ. Cal., Contract No. 4505110 (1983); J. Power Sources, $\underline{18}$, 1 (1986).

19. D. D. Macdonald and K. H. Lee, unpublished results (1982).

20. M. Pourbaix, Atlas of Electrochemical Equilibria, NACE, Houston, TX, 1974.

21. M. Urquidi-Macdonald, S. Real, and D. D. Macdonald, J. Electrochem. Soc., $\underline{133}$, 2018 (1986).

22. D. D. Macdonald and M. Urquidi-Macdonald, J. Electrochem. Soc., $\underline{132}$, 2316 (1985).

23. D. D. Macdonald, Transient Techniques in Electrochemistry, Plenum Press, NY, 1977.